



Science & Technology Facilities Council

SCARF Annual Report 2011-2012

Version: Final

Date: 16/10/2012

Edited by Peter Oliver (peter.oliver@stfc.ac.uk) 01235 441564

Content written by the respective authors

DATE	REVISION	CHANGES
15/10/12	Final	Published
05/09/12	1.2	Scientific Content Added
07/08/12	1.1	SCARF Stats, availability
07/06/12	1.0	Initial document

Abstract

Annual Report on the Usage and Scientific Impact of the SCARF Service

Dissemination

The is a public document

Contents

1. SCARF Service	4
1.1 SCARF Usage by Department	4
1.2 SCARF Availability	5
1.3 SCARF Developments 2011-12	7
1.4 Future Development	7
1.5 Help and Support	7
2. Publications and Presentations	8
2.1 Publications	8
2.2 Presentations	8
2.3 Courses	8
3. Science Highlights	8
3.1 Stewart F. Parker (ISIS)	8
3.1.1 Inelastic neutron scattering spectroscopy (INS)	8
3.2 J. C. Crabtree, S. C. Parker (University of Bath), J. A. Purton (STFC, Daresbury)	11
3.2.1 GCMC simulations of CO ₂ adsorption in zeolites	11
3.3 AR Bell (Oxford, CLF)	13
3.3.1 Magnetic field amplification driven by energetic particle streaming.	13
3.4 James Holloway (UCL, STFC-CLF)	15
3.4.1 Diamond Simulations.	15
3.5 Gabriella Graziano (University College of London), Jiří Klimeš (University College of London), Felix Fernandez-Alonso (ISIS), Angelos Michaelides (University College of London)	16
3.5.1 Density functional theory study of the interaction of molecular hydrogen and soft layered materials	16
3.6 Rob Williamson (ISIS)	19
3.6.1 Longitudinal Beam Dynamics Simulations of ISIS and its Upgrades	19
3.7 Sanghamitra. Mukhopadhyay (ISIS)	21
3.7.1 Understanding Atomic Scale properties of Functional Materials using Density Functional Theory	21
3.8 AJ Ramirez-Cuesta (ISIS)	24
3.8.1 Studying dynamics using Inelastic Neutron Scattering and Computer Modelling: Neutron Scattering and the Environment	24
3.9 Dean Adams (ISIS)	26
3.9.1 High Intensity Beam Studies on the ISIS Synchrotron using ORBIT.	26
3.10 David S.D. Gunn, Ilian T. Todorov, John A. Purton (CSED)	28
3.10.1 Defect Formation and Oxygen Vacancy Migration in Gd ₂ Ti ₂ O ₇ and Gd ₂ Zr ₂ O ₇ Pyrochlores	28
3.11 C. W. Yong (CSED) and R. Strange (Molecular Biophysics Group, Faculty of Health and Life Sciences, University of Liverpool)	29
3.11.1 Computational Studies of motor neuron disease mutants of Cu,Zn superoxide dismutase (SOD1) - insight into mechanisms of toxicity.	29
3.12 A.P.L.Robinson, Plasma Physics Group, (CLF)	30
3.12.1 Ultra-intense lasers	30
3.13 Bin Qiao (QUB), Macro Borghesi (QUB), Matthew Zepf (QUB), David Neely (RAL)	31
3.13.1 Scarf usage summary of Queens University Belfast plasma physics in 2012	31
3.14 Rowan Hargreaves (ISIS)	35
3.14.1 Measuring the effect of temperature on micelle structure using wide Q-range neutron diffraction	35
3.15 E. Higson^{1,2}, R. Trines², R. Bingham^{2,3}, and P.A. Norreys^{1,2,4} [1]University of Oxford [2] Central Laser Facility, [3] University of Strathclyde, [4] Imperial College London.	37

3.15.1	The role of phase front deformation on the growth of the filamentation instability in laser-plasma interactions	37
1.	APPENDIX : SCARF Hardware Details	41
2.	APPENDIX: Index of Figures	41
3.	APPENDIX: Publications and Presentations	43
4.	APPENDIX: SCARF Queue Usage 2011-12	47
4.1	General SCARF Queue	47
4.2	SCARF-Lexicon[1-2] Queues	48
4.3	SCARF-IBIS	49
4.4	SCARF Total Power draw (amps)	49
4.5	Filesystem Usage	50
4.6	Networking	51
5.	Appendix – SCARF Developments	52
5.1	Technical Developments	52
5.2	Application Stack	53
5.3	Staff Movements	53

1. SCARF SERVICE

SCARF is a High Performance Cluster for STFC staff, Facilities (ISIS, DIAMOND, CLF) and their users. The SCARF Service was started in 2004 and has been upgraded year on year and now represents a significant capital investment in High Performance Computing. Overall SCARF now has over 2700 CPU cores, 6.7TB memory and 100TB of diskspace (Details in Appendix 1). This report covers the year 2011-12 and outlines the research that SCARF has enabled.

1.1 SCARF Usage by Department

Each time a researcher uses the SCARF service the CPU time used is recorded. In total over 47,000 jobs, using 7.89M CPU hours, were submitted to SCARF during 2011-12.

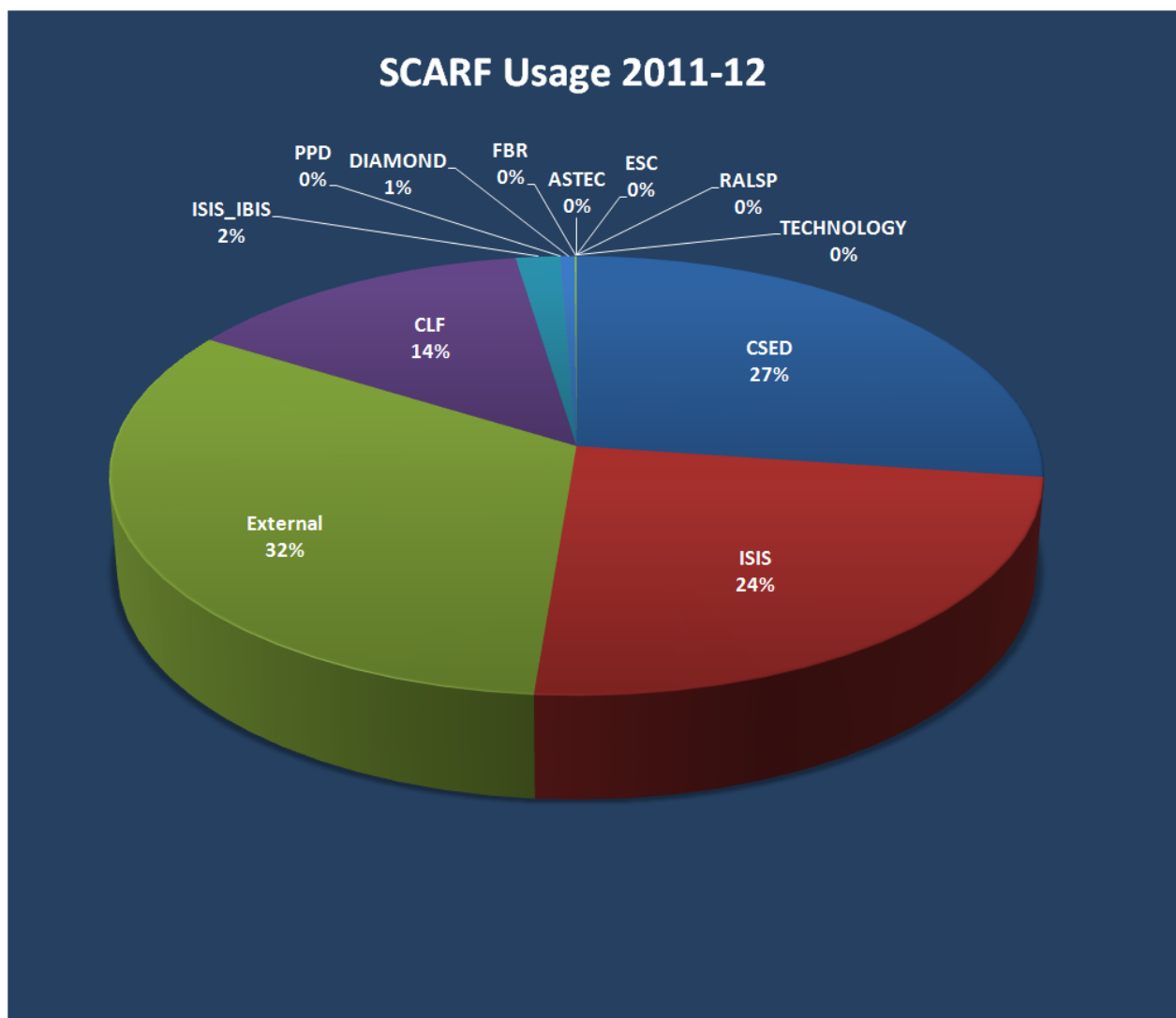


Figure 1: Pie chart showing percentage usage of the SCARF service by department

It is clear from the usage chart that ISIS and CSE are the largest users of SCARF. The External Use category measures the usage from STFC collaborations with Glasgow University, Imperial College, Bath University and Queens University Belfast.

Dept	2011-12			2010-11			2009-10		
	Active Users	CPU hrs	%	Active Users	CPU hrs	%	Active Users	CPU hrs	%
CSE	17	2151143.9	27.3	17	2194047.5	35.9	13	2635127.2	43.1
ISIS	17	1895822.3	24.0	19	1357940.5	22.2	12	1272635.2	20.8
External	6	2571711.1	32.6	7	1471784.9	24.1	7	856648.8	14.0
CLF	13	1086765.3	13.8	7	908121.6	14.9	3	392931.1	6.4
ISIS_IBIS	8	136678.1	1.7	5	104702.8	1.7	4	258576.5	4.2
PPD	1	436.8	0.0	1	44299.4	0.7	1	338.4	0.0
DIAMOND	3	45814.3	0.6	3	26503.5	0.4	1	2433.4	0.0
FBR	0	0.0	0.0	1	587.3	0.0	1	25.5	0.0
ESC	10	5394.6	0.1	7	244.5	0.0	9	25978.5	0.4
ASTEC	0	0.0	0.0	2	0.6	0.0	2	26035.7	0.4
RALSP	0	0.0	0.0	1	2.2	0.0	1	7.1	0.0
TECHNOLOGY	0	0.0	0.0	1	1577.2	0.0	1	0.0	0.0
Totals	75	7893766.3	100.0	71	6109811.8	100.0	55	5470737.5	

Figure 2: Table displaying detailed usage from 2011-12 comparing with 2010-11 and 2009-10

A significant amount of computational resource has been used on SCARF, section 3 highlights some of the scientific achievements that have been enabled.

1.2 SCARF Availability

The incident log for the SCARF service is given below:

- 24th August - scheduled downtime of 4 hours for all nodes for Panasas work
- 1st-3rd October - unscheduled outage of Scarf08 09 and Scarf-IBIS hosts due to problem with Nortel Switch Stacks
- 23rd November - scheduled downtime of 2 hours for scarf.rl.ac.uk reinstallation - cluster not affected
- 22nd December - 2 hours unscheduled downtime of Scarf09, Scarf-IBIS and part of Scarf10, due to inadvertently realistic testing of emergency shutdown procedure
- 30th January - scheduled downtime of 30 minutes for reboot of scarf.rl.ac.uk - cluster not affected
- 12th-14th March - scheduled downtime for Panasas home directory migration
- 15th March - scheduled downtime of SCARF 11 for rack move
- 16 April - unscheduled downtime due to SAN problem
- 19th-23rd April - unscheduled downtime due to Panasas problem

- 4th May - 5 hour unscheduled downtime due to SAN storage affecting VMWare
- 10th May - 3 hour unscheduled downtime due to LSF issue
- 12th-13th June - 24 hours unscheduled downtime for SCARF-LEXICON hosts due to switch failure
- 17th-19th June - unscheduled outage due to Panasas problems
- 31st July - scheduled downtime for Panasas firmware update
- 1st August -unscheduled extension to previous downtime due to problems

In Summary 78.5 hrs lost due to scheduled downtime and 370 hrs due to unscheduled outages. The major source of downtime during 2011-12 was the Panasas filesystem. There was a serious bug in the Panasas software that would appear to take the filesystem offline to fix it when it didn't need fixing. No user data was lost during these incidents but the filesystem was unavailable to users. The Panasas Software update at the end of July fixed this issue.

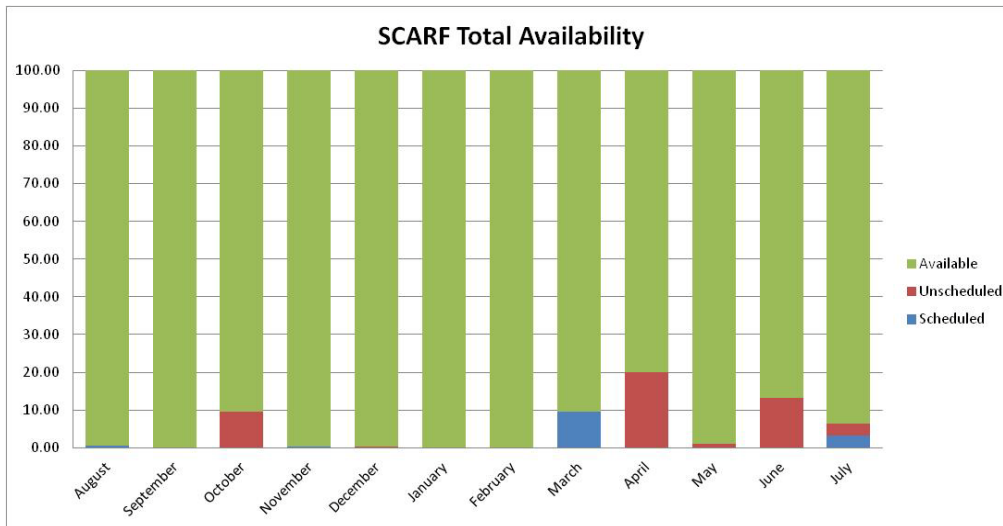


Figure 3: Availability for SCARF

The table below details the hardware availability of compute nodes by purchase date. It is evident that the older equipment purchased in 2006 is giving the most problems. This supports the rolling upgrade of SCARF and the 2006 equipment will be phased out for general use in 2012-13.

Year Purchased	Compute node Availability 2011-12	Compute node Availability 2010-11	Compute node Availability 2009-10
2006	93.5%	94.3%	94.2%
2007	98.6%	99.4%	98.5%
2008	97.9%	98.6%	99.2%
2009	99.2%	99.8%	98.4%
2010	99.9%	99.7%	98.8%
2011	99.7%	100.00% (3 Months)	NA
2012	99.9% (5 Months)	NA	NA

Figure 4: Availability vs Year Purchased

1.3 SCARF Developments 2011-12

- Major SCARF Developments are listed below. A more detailed list can be found in Appendix 5
 - New capacity added
 - 192 Intel X5675 CPU cores for general use went into production in March 2012
 - 48 Intel X5675 CPU cores for general use purchased by ISIS (Stuart Ansell) went into production in March 2012

1.4 Future Development

- SCARF 2013 Hardware Upgrade
 - ~300 CPU Cores for General Use

1.5 Help and Support

For any queries concerning the SCARF service please email the SCARF Helpdesk;
scarf@hpc-support.rl.ac.uk

2. PUBLICATIONS AND PRESENTATIONS

2.1 Publications

A list of publications is given in Appendix 3. A way of estimating the impact that SCARF has had is to analyse the Journal Impact Factor using the Journal Citation Reports published by Thomson Reuters (2011). The average Impact Factor for Journals published as a result of using SCARF is 4.4. This compares to an average impact factor across all 8200 journals of 2.07. This is a simplistic analysis but demonstrates that the science done on SCARF is having a significant impact.

2.2 Presentations

Scientists have presented their work at 15 international conferences (Appendix 3). This helps to demonstrate that the science enabled by SCARF is world class.

2.3 Courses

ISIS ran their annual Neutron training course with 10 students, using the Material Studio gateway on SCARF for the Computational Methods section of the course and used 310 CPU hrs.

3. SCIENCE HIGHLIGHTS

3.1 Stewart F. Parker (ISIS)

3.1.1 *Inelastic neutron scattering spectroscopy (INS)*

Energy is a priority area of RCUK and a strategic goal of STFC. We have used SCARF to analyse two systems that are relevant to this theme: a series of C₅ molecules important in catalysis and the low-energy modes in platinum diimine complexes that are germane to solar energy conversion. The ISIS Facility at RAL is the world-leading centre for neutron vibrational (INS) spectroscopy of materials. One of the advantages of INS is that it is straightforward to compare the results of *ab initio* calculations with the experimental data. This is a synergistic process: comparison of observed and calculated spectra is an exacting test of the calculation, while the calculation provides unambiguous assignments of the spectra. On SCARF, for the C₅ work we have used predominantly Gaussian 03 and for the Pt complexes we have used periodic density functional theory using the CASTEP code. In both cases, the work was only feasible because of the availability of SCARF.

Industrial alkene chemistry covers a wide range of chemical processes. C₂ - C₄ alkenes dominate, although higher alkenes (C₅ to ca. C₁₈) are also industrially significant, with straight chain alkenes being particularly desirable because of their link to biodegradability. The alkenes are produced by selective hydrogenation of a mixed stream that contains a range of chain lengths. As a model of this system, we have investigated the hydrogenation of unsaturated C₅ molecules over a palladium catalyst. By monitoring the gas phase species by infrared spectroscopy, it is possible to obtain molecular and isomeric specification. However, key to this process is a reliable assignment of the spectra of the individual components and this was sketchy for the C₅ systems of interest here. Figure 5 shows a scheme for the hydrogenation of the C₅ species, the mixed feedstock of *cis*- and *trans*-1,3-pentadiene plus cyclopentene as an impurity approximates to a C₅ raffinate from a refinery. We have used a combination of infrared, Raman and INS spectroscopy to obtain complete spectra of all the molecules highlighted in red in Figure 5. *Ab initio* calculations of the potential energy surface, geometry, and vibrational transition energies were performed and simulations of the vibrational

spectra compared to the experimental data, which enabled us to make complete vibrational assignments for all of the species of interest.

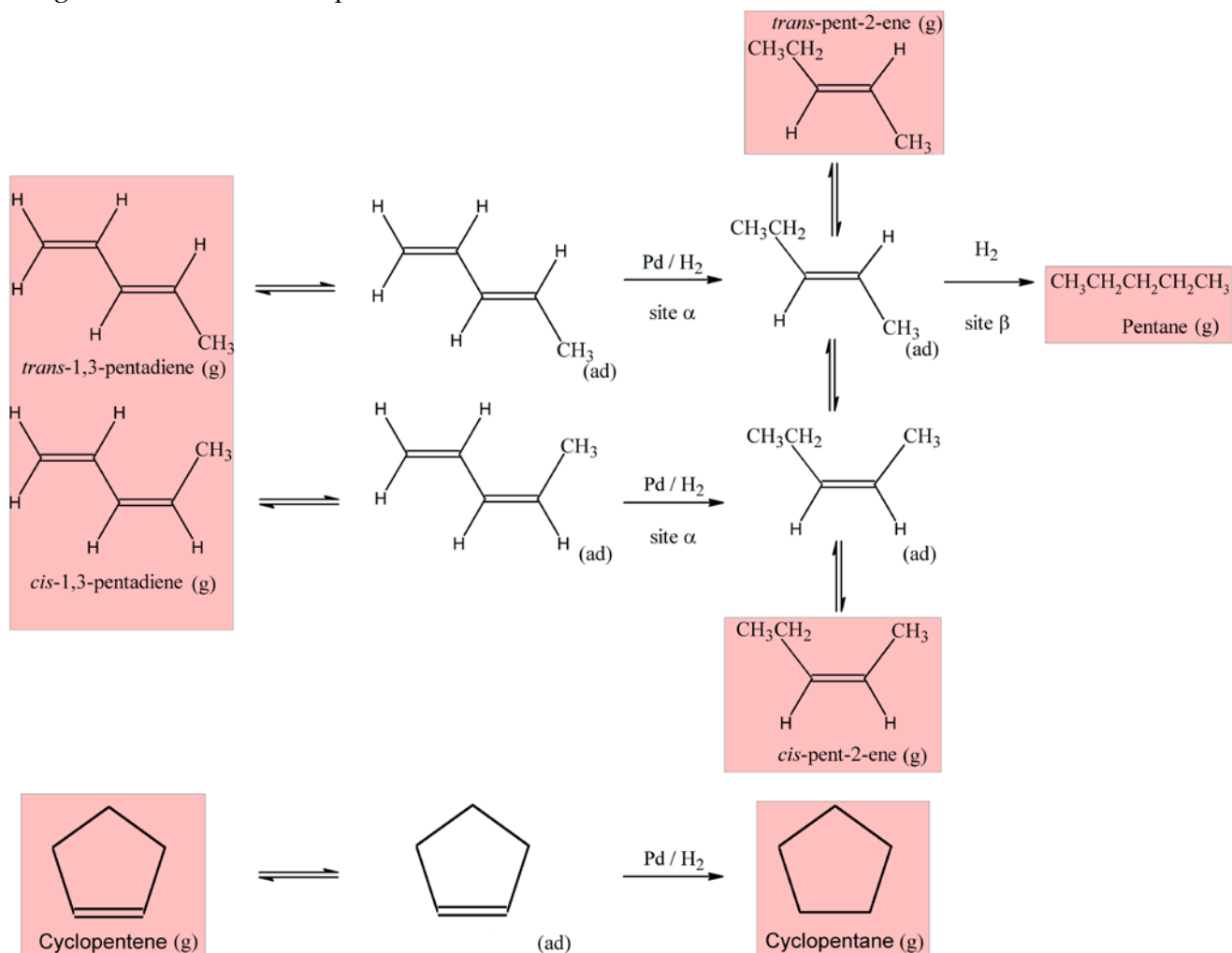


Figure 5: Scheme of the C5 species present over a working Pd/Al₂O₃ hydrogenation catalyst utilizing a mixed *cis*- and *trans*-1,3-pentadiene feedstock that contains cyclopentene as an impurity. Gas-phase species are denoted by (g) and adsorbed species by (ad). Assignment of the vibrational spectra of the molecules highlighted in red were provided by Gaussian 03 calculations on SCARF.

In solar energy conversion, the key transient is a charge-separated excited state which is formed as a result of photoinduced charge transfer following the initial absorption of photons. Pt(II) diimine complexes with ancillary anionic ligands are frequently used as the light-absorbing part of extensive molecular assemblies designed for photoinduced electron transfer in applications such as dye-sensitized solar cells and hydrogen production. An as yet unanswered question, in relation to charge-transfer excited states is their deactivation pathways. It is widely accepted that low frequency vibrational modes play an important role in the vibrational energy redistribution and energy dissipation in the excited state. In this context, metal-ligand framework vibrational modes – such as Pt–S, Pt–N or Pt–Cl vibrations - are of major importance in fundamental questions of structure and dynamics. The assignment of the ground state vibrational spectrum is an essential first step towards the assignment of the excited state spectra. A comprehensive assignment of the vibrational spectra of the ground state of the platinum 2,2'-bipyridine (bpy) thiolate (SPh) complex, Pt(bpy)(SPh)₂ as a prototype structure for a diversity of Pt(II) diimine chromophores was carried out. To assist in the analysis, comprehensive assignments of the vibrational spectra of diphenyl

disulfide, 2,2'-bipyridine and $\text{Pt}(\text{bpy})\text{Cl}_2$, the 'building blocks' of the complex were also performed. The modes of particular interest, Pt-S, Pt-N and Pt-Cl vibrations, all lie below $\sim 500\text{ cm}^{-1}$ which is readily accessible with Raman and INS spectroscopies. The analysis was complicated by the lack of a crystal structure for $\text{Pt}(\text{bpy})(\text{SPh})_2$, the structure of which had to be first determined by CASTEP, see Figure 6 left part. Subsequent comparison of the observed and calculated INS spectra, see Figure 6 right part, gave confidence in both the structure and the assignments.

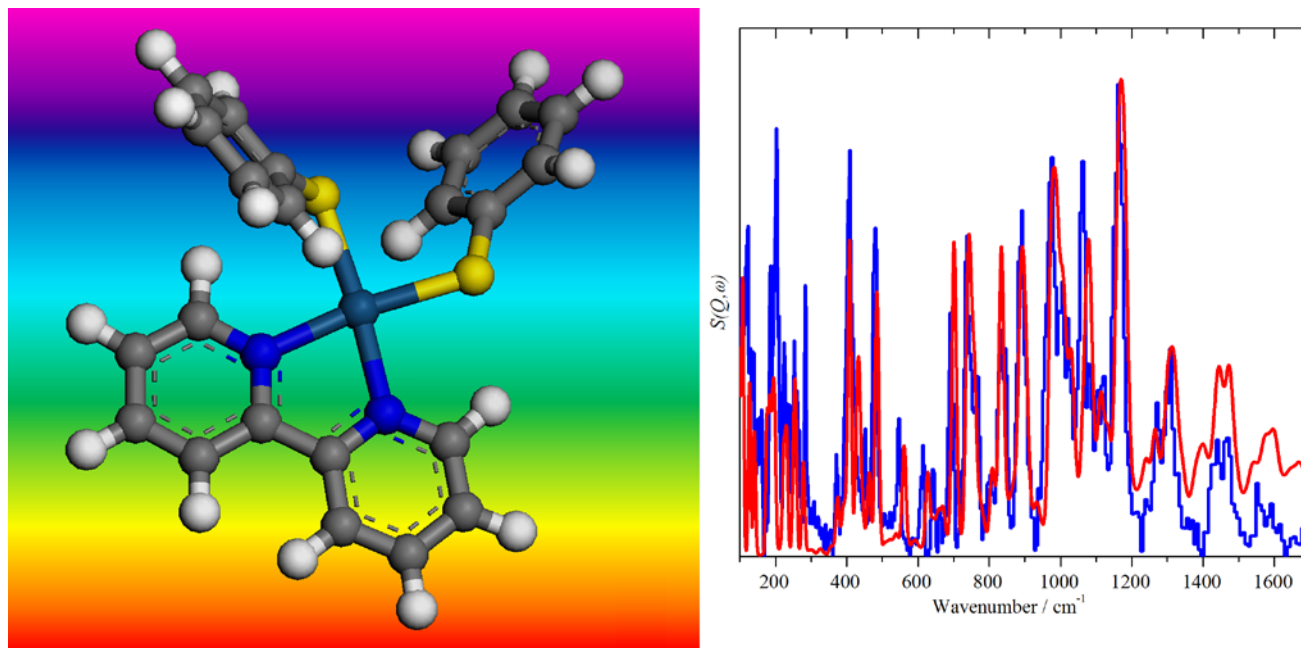


Figure 6: Left: the CASTEP geometry optimised structure of 2,2'-bipyridyl (bis)thiolate platinum (II), $\text{Pt}(\text{bpy})(\text{SPh})_2$ calculated on SCARF. Right: Comparison of the INS spectrum of the complex generated from the structure shown on the left (blue trace) with that measured on TOSCA at ISIS (red trace).

3.2 J. C. Crabtree, S. C. Parker (University of Bath), J. A. Purton (STFC, Daresbury)

3.2.1 GCMC simulations of CO₂ adsorption in zeolites

We use the SCARF cluster to run grand canonical Monte Carlo (GCMC) simulations using the DL_MONTE code. Our work focuses on the adsorption of carbon dioxide in zeolites, to identify suitable materials for sequestration. Flue gases often contain water, which is preferentially adsorbed, so it is also of interest to model the competitive adsorption to find a material which will selectively adsorb CO₂.

GCMC simulations are used to generate adsorption isotherms, which show the amount of CO₂ adsorbed as a function of pressure. Results show that our potential model (modified CLAYFF and EPM2) accurately reproduces experimental CO₂ isotherms for siliceous zeolites. This is extended to cover aluminosilicate zeolites, with counter-cations including Na⁺, K⁺ and Ca²⁺. The working potential model can now be used to predict the adsorption properties of CO₂ in any zeolite.

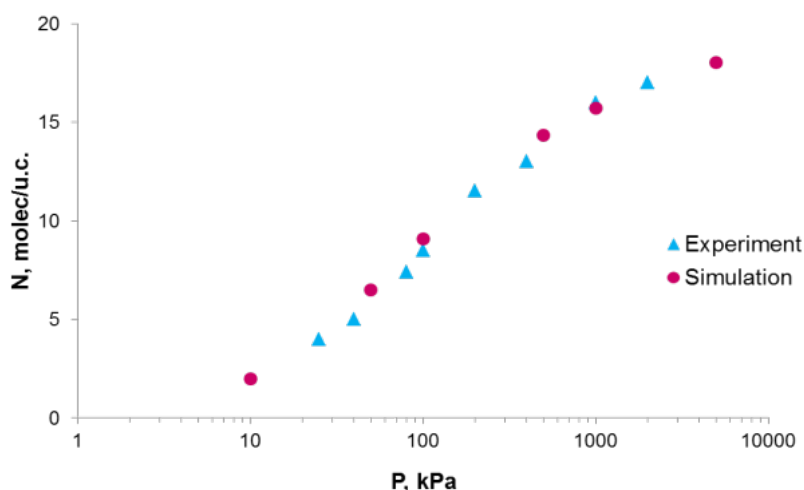


Figure 7: Adsorption of CO₂ in siliceous MFI at 308K, comparing experiment¹ to simulation

We are also studying the transport properties of CO₂ in slabs of zeolite using the DL_POLY code. We use molecular dynamics to investigate the diffusion of CO₂ through slabs with a range of interfaces, to show the impact they can have on the transport properties.

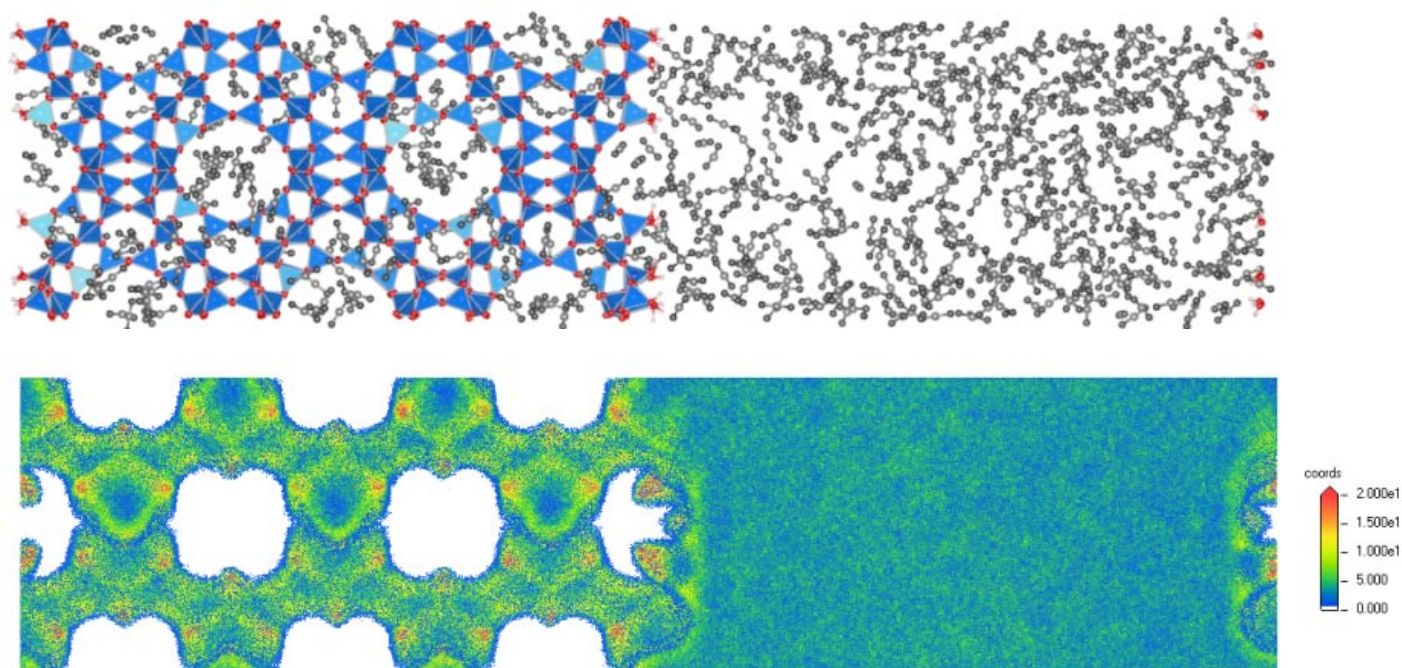


Figure 8: {011} siliceous FAU slab filled with CO₂ (top). Diffusion density profile of CO₂ in this slab (bottom), where red represents the favoured adsorption sites.

Preliminary work has been carried out on the adsorption of water in zeolites, comparing the adsorption isotherms for water potentials (SPC/FW and TIP3P/FS) to find which is most suitable for our purposes. Competitive adsorption of CO₂ and water can then be modelled, to find candidates that adsorb CO₂ preferentially over water.

[1] A. Garcia-Sanchez *et al.*, J. Phys. Chem. C, **113**, 8814-8820, 2009

3.3 AR Bell (Oxford, CLF)

3.3.1 *Magnetic field amplification driven by energetic particle streaming.*

Laboratory astrophysics is a growing subject, particularly in relation to experiments on high power lasers such as those available at the Central Laser Facility. In this past year an Oxford-led experiment (Gregori et al, Letter to Nature [1]) has reproduced the Biermann battery at a curved shock in a process thought to generate magnetic field in the early universe. In a recent theory paper [2] we show that resistively generated magnetic field, well known in laser-produced plasmas, may produce field in the voids between primordial galaxies. A further class of potential laser-plasma experiments builds upon the equivalence between energetic electron transport in the laboratory and cosmic ray acceleration at supernova shocks. Energetic electrons and cosmic rays are both described by the Vlasov-Fokker-Planck (VFP) equation [3]. This year we have used SCARF to solve the VFP equation for plasma instabilities driven by energetic particles. This is a computationally intensive procedure requiring novel numerical methods developed specifically to model time-dependent non-linear instability in six-dimensional configuration and momentum space. The simulation models the interaction of the energetic particles (modelled by the VFP equation) with a background plasma (modelled magnetohydrodynamically in 3D). Figure 9 shows the results of one simulation. A shock advances into the plasma from the right hand boundary. The particles gain energy at the shock and attempt to stream ahead of the shock. The streaming particles excite a plasma instability which generates magnetic field [4]. Spatial fluctuations in the magnetic field scatter the particles, inhibiting their streaming and confining them near the shock. The computer code solves the equations in a dimensionless form so the same model can be applied to both laboratory and astrophysical plasmas. In the astrophysical context the energetic particles are protons with energies of the order of 100TeV streaming ahead of supernova blast wave into the interstellar medium with a density of $\sim 1 \text{ cm}^{-3}$ and a magnetic field of a few microGauss. In the laboratory context, the energetic particles are electrons with energies of the order of 1MeV produced by laser-solid interactions and streaming into a plasma with a density of $\sim 10^{18} \text{ cm}^{-3}$ and a magnetic field of $\sim 10 \text{ kG}$. The relevant timescales are 100s of years in the astrophysical case and nanoseconds in the laboratory case. In this way, it should be possible with the aid of numerical simulation to validate a key aspect of high energy astrophysics in the laboratory.

[1] Generation of scaled protogalactic seed magnetic fields in laser-produced shock wave.

Gregori G; plus 26 authors, Nature 481, 480-483 (2012)

[2] Resistive Magnetic field Generation at Cosmic Dawn. Miniati F; Bell AR, Astrophys J 729, 73 (2011)

[3] Fast electron transport in laser-produced plasmas and the KALOS code for solution of the Vlasov-Fokker-Planck equation. Bell AR; Robinson APL; Sherlock M; et al., Plasma Phys Cont Fusion 48, R37-R57 (2006)

[4] Turbulent amplification of magnetic field and diffusive shock acceleration of cosmic rays.

Bell AR, Mon Not R Astr Soc 353, 550-558 (2004)

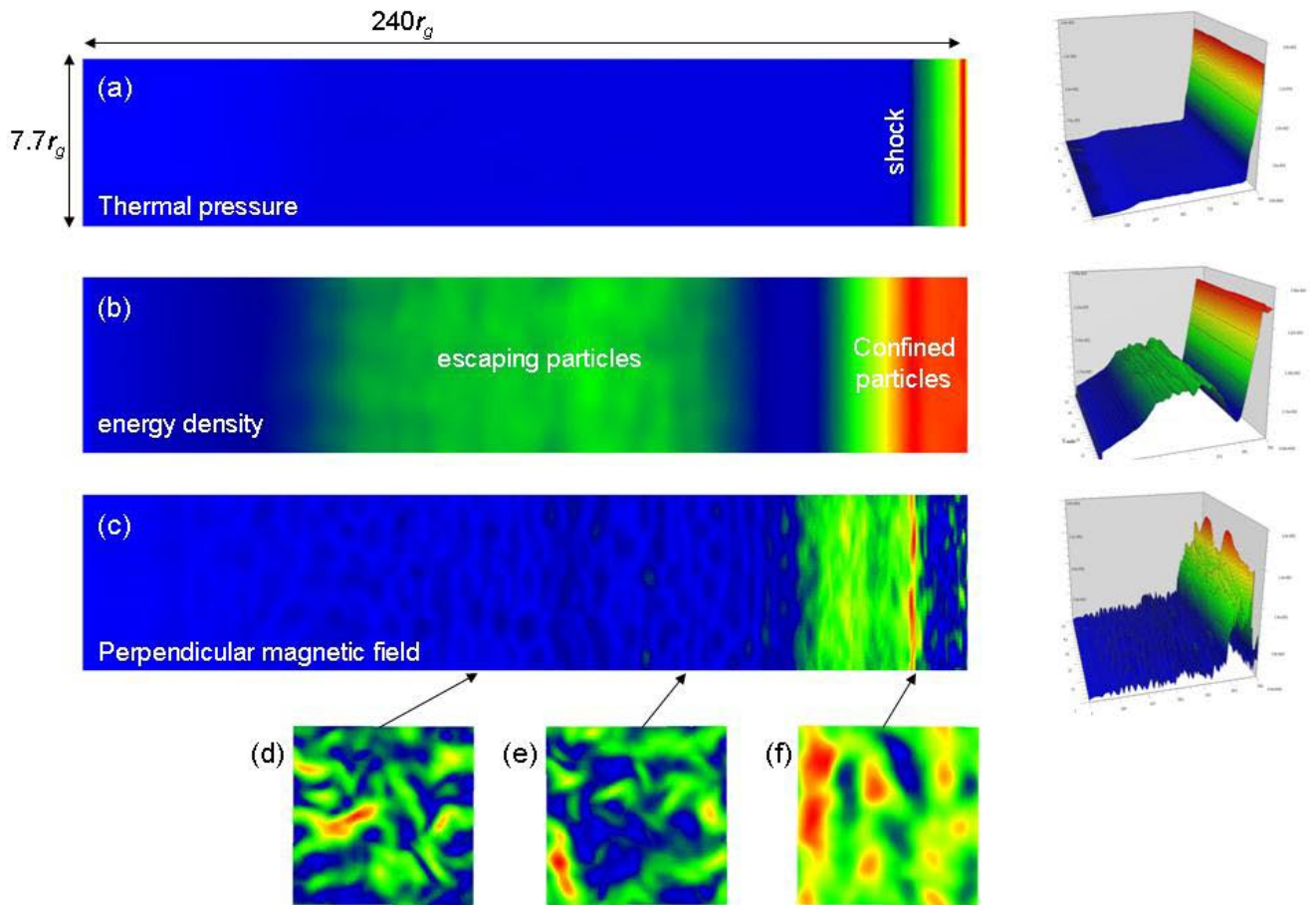


Figure 9: Interaction of energetic particles with a magnetohydrodynamic (MHD) background plasma: (a) Background thermal pressure with a shock advancing from the right (b) energy density of energetic particles showing that some particles escape ahead of the shock and generate magnetic field that confines other particles at the shock (c) magnitude of the magnetic field excited by streaming energetic particles. The panels to the right display the same information in a different format. (d-f) show the structure of the magnetic field perpendicular to the direction of particle streaming.

3.4 James Holloway (UCL, STFC-CLF)

3.4.1 Diamond Simulations.

The Diamond simulation set aims to determine the viability of using the 3 GeV Diamond electron beam, at RAL, to drive plasma wakefield acceleration. If feasible, the Diamond beam could be used to generate a witness electron beam of 6 GeV and generate hard x-rays whilst experimentally demonstrating the self modulation instability for the first time.

The Diamond simulation set is at a mature stage. Many configurations have been explored, and have led to the current set up of an ultra short high intensity laser pulse leading the Diamond beam into the plasma. The laser pulse drives an initial high amplitude wakefield which seeds the self modulation instability, enhancing its growth rate. Once modulated, the Diamond beam can drive a significant wakefield which can then be utilised.

The bulk of the remaining simulations comprise of a parameter scan over laser intensity to optimize the seeding of the self modulation instability followed by a full length simulation of the optimized parameters.

If feasible for the Diamond beam, plasma cells could be added to other existing synchrotron / linac facilities, potentially doubling the beam energy. The cells would only need of the order of a meter of beam line. The plasma cell and seed laser are relatively inexpensive considering the potential gains.

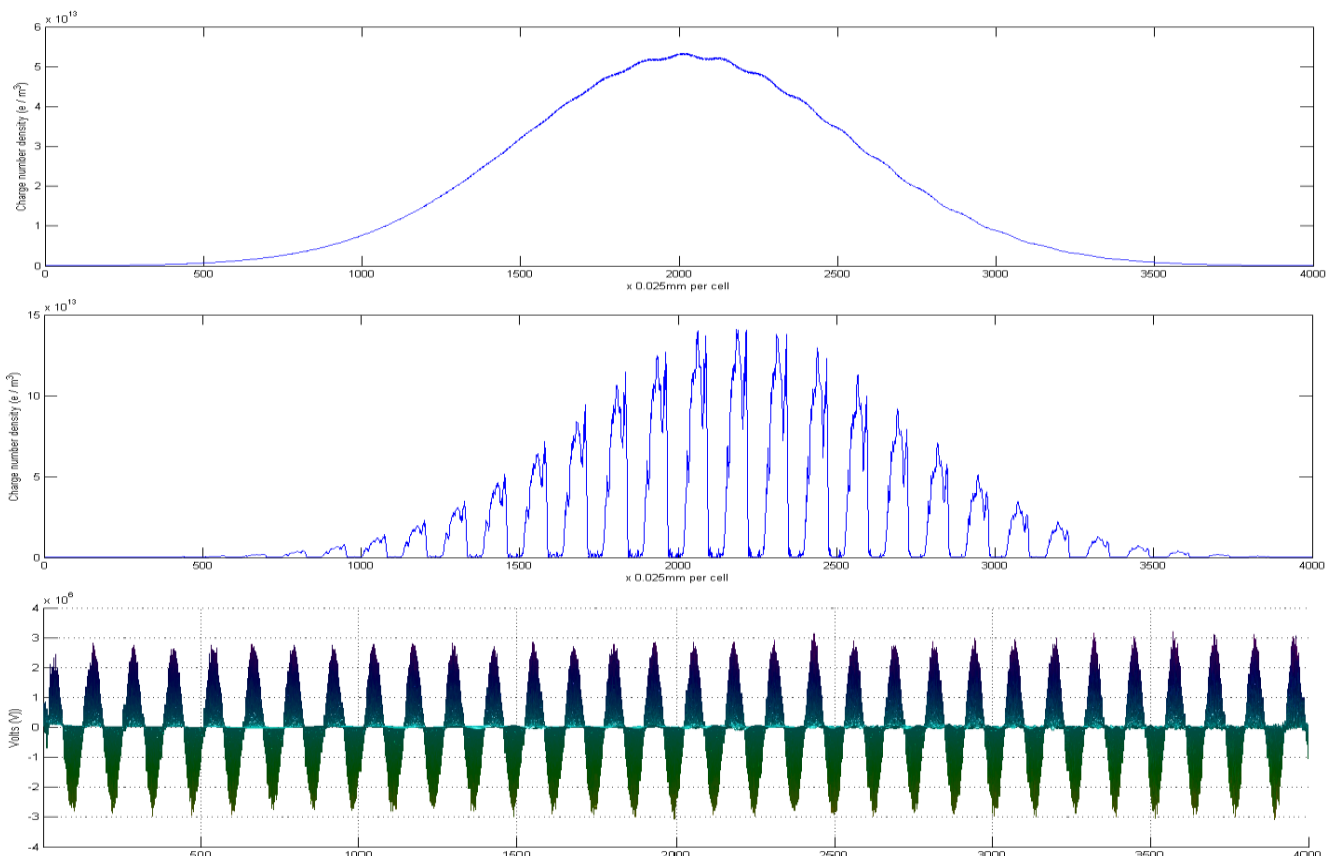


Figure 10: The Diamond beam before propagating through the plasma cell (top), after the plasma cell where microbunches are visible (middle) and the wakefield that has microbunched the beam (bottom).

3.5 Gabriella Graziano (University College of London), Jiří Klimeš (University College of London), Felix Fernandez-Alonso (ISIS), Angelos Michaelides (University College of London)

3.5.1 Density functional theory study of the interaction of molecular hydrogen and soft layered materials

Our calculations on the SCARF cluster have been focused on the description of the adsorption of hydrogen on and in soft layered materials, like graphite and hexagonal-boron nitride. To this end, we have carried out density functional theory (DFT) calculations using a new functional: the optimized Becke88 van der Waals (optB88-vdW). [1]

The interaction between hydrogen and soft layered materials is dominated by van der Waals dispersion forces which are not captured by standard DFT functionals (LDA and GGA). The optB88-vdW belongs to the class of functionals known as vdW-DFs, [2] which have been designed to account properly for dispersion forces. It has been already successfully tested for the description of the interlayer properties of graphite and *h*-BN, which are also dominated by vdW forces. [3] These results gave us confidence to apply the optB88-vdW for the study of more complex systems like hydrogen interacting with soft layered materials.

We performed our calculations using the plane-wave basis set code VASP 5.2 and the optB88-vdW exchange-correlation functional with PBE-optimized projector-augmented-wave (PAW) potential. In order to understand how important dispersion forces are, we compared the optB88-vdW results to those obtained with the standard PBE functional.

We first looked at different adsorption sites for molecular hydrogen on graphene and a single layer of *h*-BN. We found that the adsorbed molecule does not have a strong preference for any position or orientation on both materials, as shown in Fig.11. We also found that the adsorption energy of the hydrogen is pretty much the same on both substrates. Fig. 11 also highlights how the omission of dispersion forces in PBE leads to a clear underestimation of the total adsorption energy

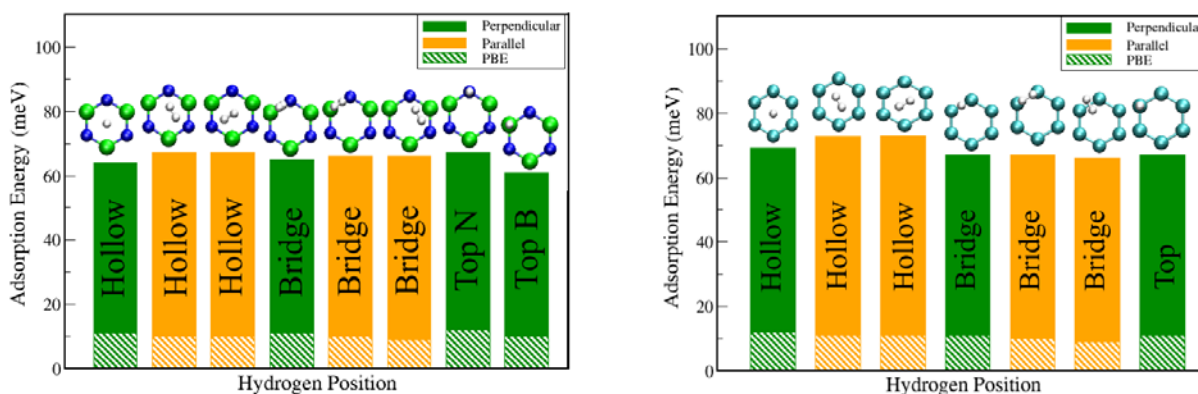


Figure 11: Adsorption energies of hydrogen on graphene and a single-layer of *h*-BN. Each histogram refers to a different configuration of the molecule on the substrate. The solid part of the histograms refers to the results obtained with the optB88-vdW functional, while the bottom part refers to the PBE results.

We then studied the absorption of hydrogen in bulk graphite and *h*-BN, to try to infer the optimal interlayer spacing for both materials in order to host the gas molecule. The results reported in Figure 12 show how both materials need to expand their interlayer distance from ~ 3.3 Å to ~ 5.5 Å, and that the interlayer binding energy is substantially screened by the presence of the hydrogen molecule.

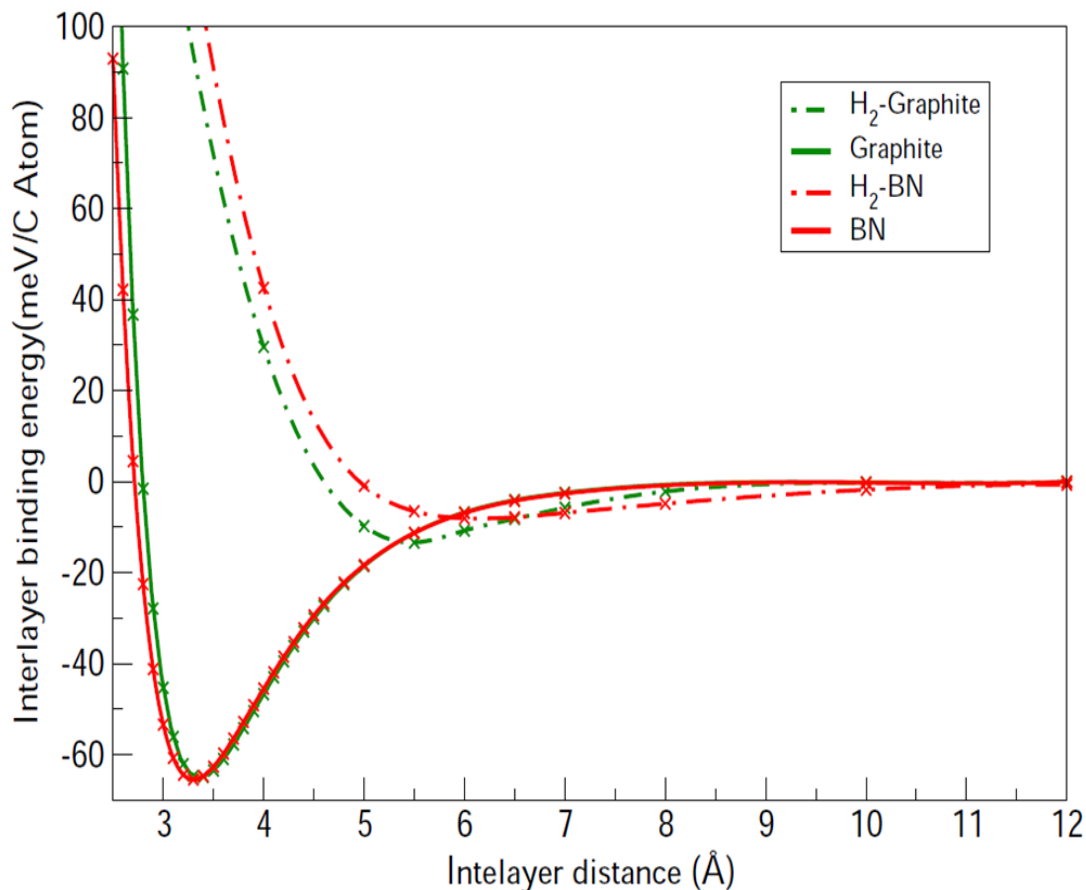


Figure 12: The solid lines refer to the interlayer binding curves of graphite and *h*-BN. The dashed curves refer to the interlayer binding of the two materials when an hydrogen molecule is absorbed between the layers. The dashed curves clearly highlight the expansion of the interlayer spacing of the two materials due to the absorption of the gas molecule and a subsequent decrease of the binding energy.

The expansion of the interlayer spacing in graphite and *h*-BN has an energetic cost, which makes the whole absorption process endothermic (~ 1 eV/H₂ mol). In Fig. 13 we show how these energetic costs are substantially reduced if a pre-expanded material is used, leading to an adsorption energy per hydrogen molecule of ~ 150 meV/H₂ mol.

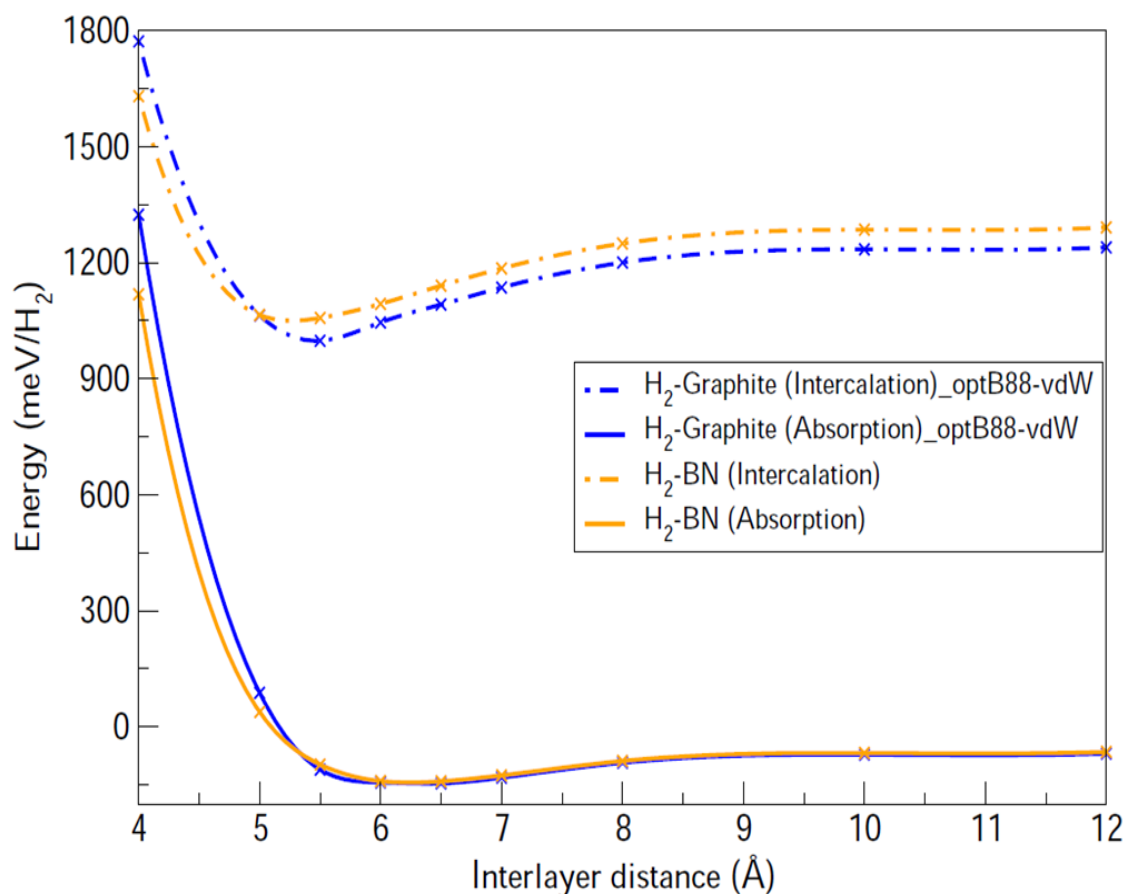


Figure 13: The dashed curves represent the absorption energy per hydrogen molecule as a function of interlayer spacing in graphite and h-BN, where the interlayer distance is ~ 3.33 Å. The solid lines refer to the absorption energy per hydrogen molecule in the pre-expanded materials.

These results provide important insights into the search of a suitable intercalant that minimises the energetic costs associated with the absorption of hydrogen. These intercalants can act as molecular pillars as well as increase the interaction between hydrogen and the substrate. To this end, we are currently exploring the intercalation of metals into these layered materials using this new functional.

[1] J. Klimeš, D. R. Bowler, and A. Michaelides, *J. Phys.: Condens. Matter* 22, 022201 (2010).

[2] M. Dion, H. Rydberg, E. Schroder, D. C. Langreth, and B. I. Lundqvist, *Phys. Rev. Lett.* 92, 246401 (2004).

[3] G. Graziano, J. Klimeš, F. Fernandez-Alonso, and A. Michaelides, *J. Phys.: Condens. Matter*, Accepted.

3.6 Rob Williamson (ISIS)

3.6.1 Longitudinal Beam Dynamics Simulations of ISIS and its Upgrades

An in-house modular, C++ Particle-In-Cell (PIC) code has been developed to simulate longitudinal beam dynamics in synchrotrons, with particular application to ISIS and its proposed upgrades. In order to compare favourably with experimental observations of ISIS several longitudinal aspects of particle acceleration need to be included. The code includes modules to create beam distributions for either multi-turn or single turn injection; the capability of single or dual harmonic RF acceleration; two separate calculation methods of beam induced space charge; the ability to include other impedances as functions of frequency; several diagnostic outputs including beam moments and stability estimates.

So far, simulations have been performed for proposed megawatt (MW) upgrades to ISIS involving the addition of a new synchrotron [1], a ~0.5 MW upgrade by virtue of a 180 MeV replacement to the current 70 MeV injector [2, 3], and for the present ISIS synchrotron [3]. Results include graphs of the evolution of longitudinal profiles (Figure 14), longitudinal phase space (Figure 15, top) as well as diagnostic parameters including a measure of beam stability, the degree of bunching and bunch momentum spread as a function of time (Figure 15, bottom) as well as many others.

The longitudinal code is installed and run on SCARF on a single processor. The data produced is then passed to a desktop for further processing and visualizations. Code development is done on SCARF and there are plans for further modules to be added to the longitudinal C++ code. Current work is also focused on writing a 3D, C++ particle dynamics code by merging the longitudinal (1D) dynamics code with another in-house transverse (2D) code, Set. This code will be parallel and include multi-turn injection processes and stripping foil interactions.

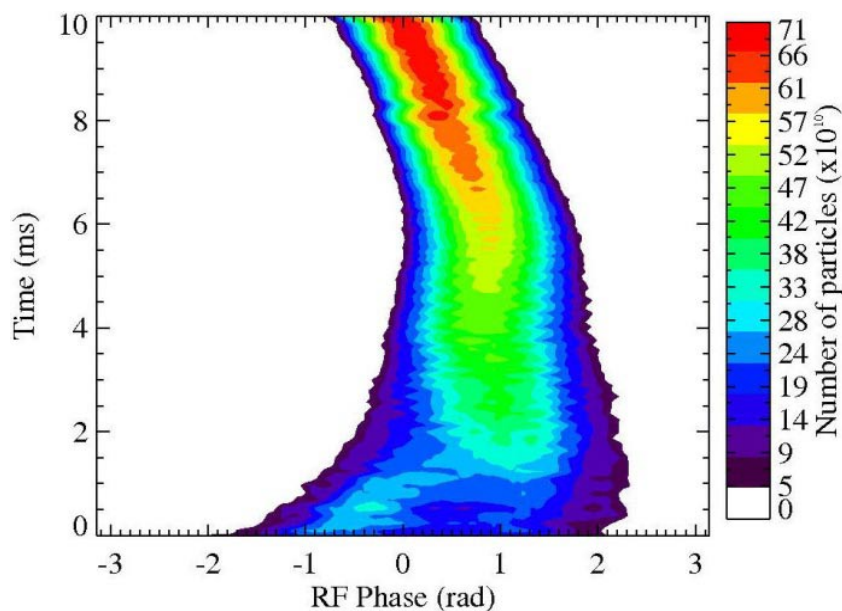


Figure 14: Evolution of longitudinal profile (mountain range) as a function of time with colour indicating particle population, for approximate ISIS parameters.

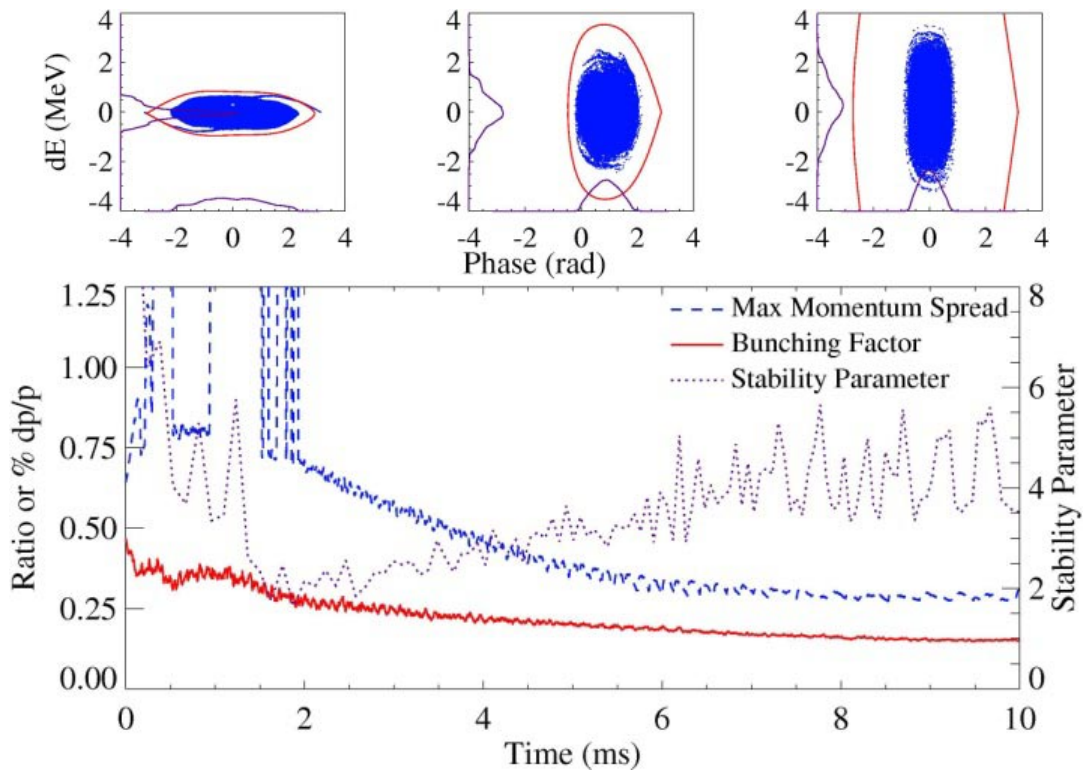


Figure 15: Longitudinal phase space (top) at the end of injection (0 ms), mid-cycle (5 ms) and just prior to extraction (10 ms) for approximate ISIS running parameters. Momentum spread, bunching factor and stability parameters (bottom) as a function of time through 10 ms cycle for approximate ISIS parameters.

[1]R.E. Williamson et al., "Longitudinal dynamics studies for ISIS upgrades", Proc. PAC09, <http://epubs.stfc.ac.uk/work-details?w=50342>
 [2]R.E. Williamson et al., "High intensity longitudinal dynamics studies for higher energy injection into the ISIS synchrotron", Proc. IPAC11, <http://epubs.stfc.ac.uk/work-details?w=60831>
 [3]R.E. Williamson et al., "High Intensity Longitudinal Dynamics Studies for an ISIS Injection Upgrade", Proc. HB2012, <http://epubs.stfc.ac.uk/work-details?w=63542>

3.7 Sanghamitra. Mukhopadhyay (ISIS)

3.7.1 Understanding Atomic Scale properties of Functional Materials using Density Functional Theory

In the last one year I have used Scarf computer for following three projects:

Effect of Background Carriers on Magnetic Interactions in Mn doped Dilute Magnetic Silicon :

Dilute magnetic semiconductors (DMS) have the potential for spintronic applications because possibility of manipulations of spins in these materials. The mature state of silicon technology offers high incentives for making silicon based DMS. Using hybrid exchange density functional calculations we show that the type of background carriers has significant effects on magnetic interactions in Mn doped dilute magnetic Si. We have used Gaussian based linear combination of atomic orbitals (LCAO) as our basis set and B3LYP hybrid exchange functionals, as implemented in the CRYSTAL code. In our calculations the p- and n-type Si were simulated by introducing an extra hole and an extra electron, respectively, in the 64 atoms Si supercell. The extra charge was compensated by a homogeneous background potential. Our calculations predict that with 1.6% Mn doping and of p-type Si the ground state is ferromagnetic, whereas other conditions remaining the same, the ground state becomes antiferromagnetic for the n-type Si. The exchange energies in Mn-doped extrinsic Si are higher by about 1 eV/Mn atom compared to the Mn doped intrinsic Si. Calculated electronic structures reveal that in p-type Si:Mn the hole localises over Mn and the short range magnetic coupling increases. On the other hand, in the n-type host electron-electron repulsion increases within Mn-Si impurity band and the short range coupling decreases destroying the long range spin polarisation. These calculations explain the observed ferromagnetism in the p-type Si:Mn at higher temperatures than in the n-type Si:Mn and the magnetic moments of the systems compare well with experiments [1].

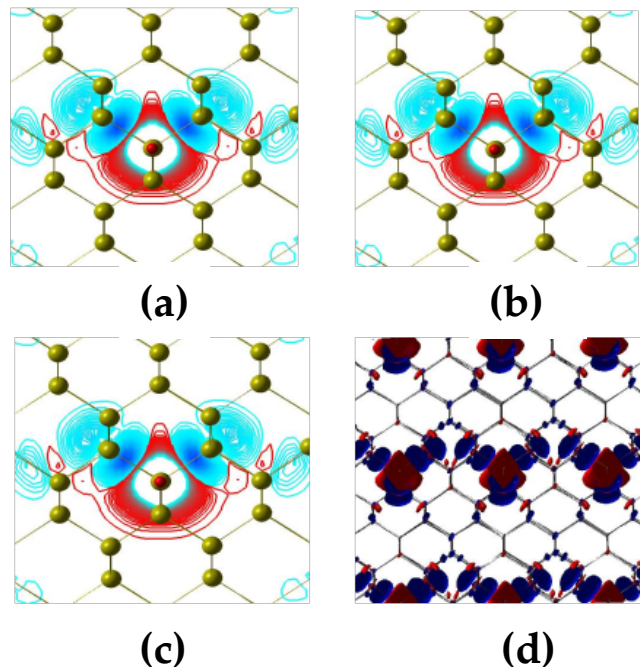


Figure 16: Spin densities on the 110 plane of the (a) intrinsic Si (b) p-type Si, (c) n-type Si host for the range of -0.02 $\mu\text{B} / \text{bohr}^3$ to 0.02 $\mu\text{B} / \text{bohr}^3$ with a step of $2 \times 10^{-4} \mu\text{B} / \text{bohr}^3$. The blue lines are for majority spin states and red lines are for minority spin states. The highest magnitude of spins for each type of spin is at the centre of contours. (d) The long range spin polarisation of the p-type Si:Mn. The range of this plot is -0.02 $\mu\text{B} / \text{bohr}^3$ to +0.0002 $\mu\text{B} / \text{bohr}^3$. The range has been modified from the former to include atoms having very small spins over them.

Electronic Structures and Thermodynamic Properties of LaCoO₃, a Material for Solid Oxide Fuel Cell : LaCoO₃ is a technologically important material in part because of its use as a cathode in a high temperature solid oxide fuel cells (SOFC). It exhibits complex and temperature-dependent electronic and magnetic properties. Below about 100K it has been reported as a nonmagnetic semiconductor, around 100-500K as a paramagnetic semiconductor and above 500K as a paramagnetic metal. We have used hybrid exchange density functional theory as implemented in CRYSTAL code to model the electronic structure of LaCoO₃. Based on a rhombohedral unit cell of R-3c symmetry containing two Co atoms we find a mixed spin phase, comprising alternating low and high spin Co⁺³ ions, with a total energy at 0K just 57meV per formula unit above that of a non-magnetic semiconducting ground state. In the mixed spin phase the high-spin Co⁺³ ion have spin moments of 3.1 μ B and the state is insulating with a band gap of 2.2eV. Our calculations suggest that the effective on-site Coulomb repulsion energy, U_{eff} , on Co⁺³ ions are spin dependent. An estimate of the harmonic phonon free energy suggests that this mixed spin phase would become the more stable phase as the temperature increases, which is consistent with experimental evidence. An alternative intermediate spin state is higher in energy at all temperatures [2].

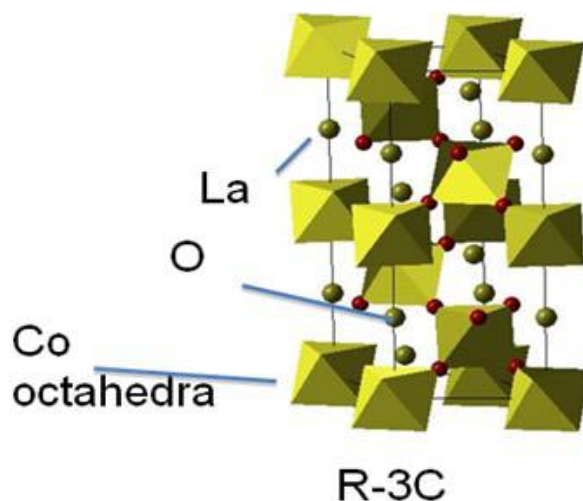


Figure 17: Rhombohedral structure of LaCoO₃

Vibrational Properties of Organic Ferroelectric Croconic Acid : Croconic Acid (C₅O₅H₂) is the first organic molecule which shows room temperature ferroelectricity in its crystalline form. The structure and vibrational properties of this crystal are important to understand its ferroelectric properties. In this investigation, we employed state-of-the-art calculations based on plane wave pseudo potential density functional theory (DFT) to predict the structure, vibrational and polarizability properties of Croconic acid and compared with in-house experiments. We investigated structures of Croconic Acid in both centro symmetric, space group Pcam, and non-centrosymmetric, space group Pca21, form using CASTEP code and dispersion corrected Perdew-Burke-Ernerhof generalised gradient approximation (PBE-GGA + D) in DFT. The experimentally obtained structures were relaxed using BFGS method and the centrosymmetric structure was found to be unstable with respect to the non-centro symmetric structure. The calculated bond lengths were in agreement with neutron diffraction results obtained from ISIS-IRIS instrument within 3%.

The calculated vibrational spectrum compared well with inelastic neutron scattering (INS), infrared (IR) and Raman spectroscopic results. The polarizability of the crystal was identified by the large anisotropy of the Born effective charge tensors associated with the hydrogen ions, which also had directional properties. We predicted that these hydrogen ions had dominant role in the ferroelectric properties of the crystal [3].

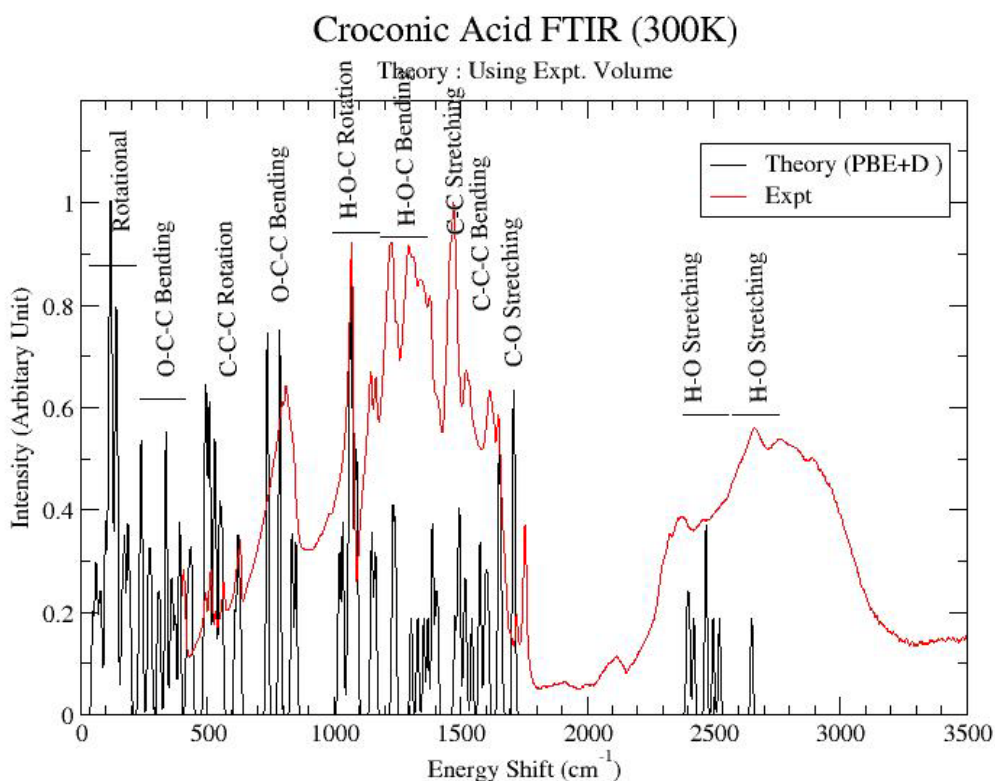


Figure 18: Density functional simulation of IR spectrum of Croconic acid compared with experiment.

- [1] S. Mukhopadhyay and N. M. Harrison, "Influence of background carriers on magnetic properties of Mn-doped dilute magnetic Si", *J. Mag. Mat.*, **324**, 3748 (2012).
- [2] S. Mukhopadhyay, M. W. Finnis and N. M. Harrison, "Electronic Structures and Phonon Free Energies of LaCoO_3 using Hybrid Exchange Density Functional Theory", to be published in *Phys. Rev. B* (2012).
- [3] S. Mukhopadhyay, M. Gutmann, D. Jochym, K. Refson and F. Fernandez-Alonso, "Crystalline Structure and Vibrational Properties of Organic Ferroelectric Croconic Acid : an Investigation using Density Functional Theory", presented in the Joint CMD-24, ECOSS-29, ECSCD-11 and CMMP-12 Conference held at Edinburgh, 3-7 September (2012).

3.8 AJ Ramirez-Cuesta (ISIS)

3.8.1 *Studying dynamics using Inelastic Neutron Scattering and Computer Modelling: Neutron Scattering and the Environment*

Amongst the toughest challenges that we face at the beginning of the 21st century is the reduction of our carbon footprint. There are different ways of achieving this, either we use different energy vectors, i.e. hydrogen storage materials or we can also sequester carbon dioxide. We know how to produce energy from a variety of sources, but there are not many efficient ways of storing such energy. The most efficient way of storing energy is in its chemical form, in batteries or as hydrogen gas. The retrieval of the stored energy is straightforward in the case of the batteries but in the case of hydrogen requires an additional step that may be performed via fuel cell (conversion to electrical energy) or by burning (conversion to thermal energy). Hydrogen can store the most energy per unit weight of any element in the periodic table, and its potential applications as an energy vector are essentially unlimited. It can be used to store energy produced from sustainable energy sources during periods of low demand, that energy then used during periods of peak demand. However, as a gas, its volumetric energy density is very low. Consequently, it is a great imperative to identify methods of storing hydrogen in high gravimetric and volumetric densities. [1,2,3].

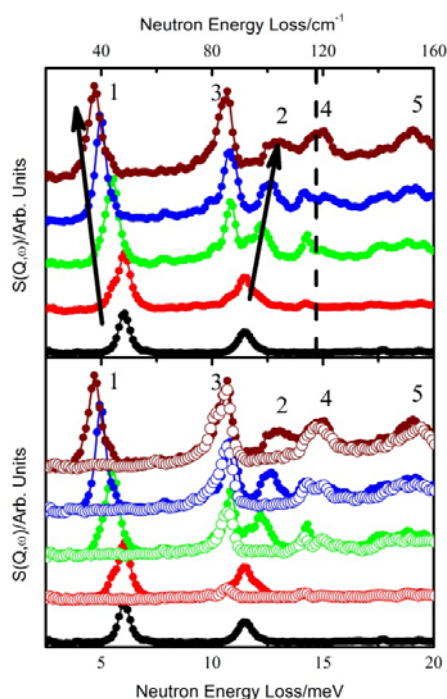


Figure 19: The INS of pH₂ in Fe MOF. Top) pure pH₂. Bottom) one equivalent load of D₂ and further pH₂. Demonstrating the existence of two sites for adsorption.[4] SCARF calculations were used to determine the DoS of the empty cage.

Carbon sequestration, on the other hand, consists of trapping the greenhouse gases from the atmosphere, i.e. from the flue gases of a power station. The efficient removal of CO₂ and SO₂ represents a major challenge in the development of the 'low-carbon economy'. At present, solutions of organic amine are widely used to capture the CO₂ generated by power plants, but the considerable costs associated with the substantial energy input required for the regeneration of the amine solutions, as well as their highly corrosive nature, significantly limit their long-term application. Powerful drivers therefore exist to develop efficient strategies to remove CO₂ using

alternative materials that simultaneously demonstrate high adsorption capacity, high selectivity and high rates of regeneration at an economically viable cost.

Porous metal–organic framework (MOF) complexes are a sub-class of coordination polymers that show great promise for gas storage and separation because of their high surface area and tunable functional pore environment. Within the field of gas capture, there is particular emphasis on optimizing the interactions between the MOF hosts and the adsorbed gas molecules, leading to the discovery of new functional materials with better capture properties. Accordingly, the identification of preferred adsorption sites within a pore structure and the direct visualization of binding interactions represent important methodologies for understanding the mechanisms for the selective capture of CO₂ and SO₂. We have used TOSCA to study by INS and DFT modelling the interactions of NOTT 300 and CO₂ and SO₂. We determined the criteria of stability by the comparison between modelling and experiment. [5]

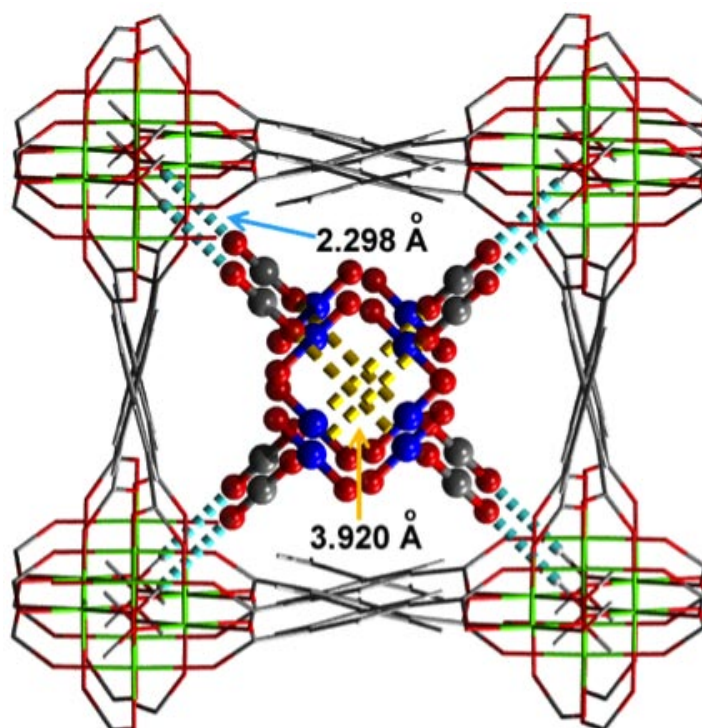


Figure 20: Determination of the absorption site of CO₂ in NOTT 300 using INS and DFT (SCARF calculations)

The vibrational properties of solids and molecules are studied by spectroscopic methods. The stability of phases is determined by the thermodynamical functions, in particular the Gibbs free energy. We have improved and developed the methodology to do that as well. [6]

- [1] Ramirez-Cuesta A, Jones M, David W. Neutron scattering and hydrogen storage. *MATERIALS TODAY*. 2009;12(11):54-61.
- [2] Albinati, A., Colognesi, D., Georgiev, P. A., Jensen, C. M. and Ramirez-Cuesta, A. J. On the effect of thermal treatment and hydrogen vibrational dynamics in sodium alanates: An inelastic neutron scattering study. *Journal of Alloys and Compounds* 523, 108–113 (2012).
- [3] Yang, S. H.; Callear, S. K.; **Ramirez-Cuesta, A. J.**; David, W. I. F.; Sun, J. L.; Blake, A. J.; Champness, N. R.; Schroder, M., Pore with gate: modulating hydrogen storage in metal-organic framework materials via cation exchange. *Faraday Discussions* **2011**, *151*, 19-36.
- [4] Queen, WL, Bloch ED, Brown CM, Hudson MR, Mason JA, Murray LJ, Ramirez-Cuesta AJ, Peterson VK, and Long JR. Hydrogen adsorption in the metal-organic frameworks Fe-2(dobdc) and Fe-2(O-2)(dobdc). *Dalton Transactions* 41, 4180–4187 (2012).
- [5] Yang S., Sun J., Ramirez-Cuesta A.J., Callear S.K., David W.I.F, Anderson D., Newby A., Blake A.J., Parker J.E., Tang C.E. and Schröder M. "Direct Visualisation of Carbon Dioxide and Sulphur Dioxide in a Decorated Porous Host" *Nature Chemistry*, DOI: 10.1038/NCHEM.1457
- [6] Borgschulte, A.; Gremaud, R.; Züttel, A.; Martelli, P.; Remhof, A.; Ramirez-Cuesta, A.; Refson, K.; Bardaji, E.; Lohstroh, W.; Fichtner, M.; Hagemann, H.; Ernst, M., Experimental evidence of librational vibrations determining the stability of calcium borohydride. *Physical Review B* 2011, 83 (2)

3.9 Dean Adams (ISIS)

3.9.1 High Intensity Beam Studies on the ISIS Synchrotron using ORBIT.

The ISIS Synchrotron forms part of the accelerator chain for the spallation neutron source. High intensity beam operation is limited by uncontrolled beam losses which activate machine components limiting hands on maintenance. Beam loss in the synchrotron is dominated by the adiabatic RF trapping process and high intensity space charge effects. Studies are underway using the particle tracking code ORBIT to understand these mechanisms to allow lower beam loss operation. Understanding high intensity mechanisms are also important in the design of ISIS upgrades and future machines.

Synchrotron beam dynamics have been modelled in the particle tracking code ORBIT on the SCARF cluster. The model tracks 2×10^6 macro particles over the first 3ms (3500 turns) of the synchrotron cycle covering the period of beam loss. The model includes injection painting dynamics, injection foil physics, RF acceleration, RF errors, collector systems, vacuum vessel apertures and 2.5D space charge. The model is fitted to longitudinal measured profiles through the acceleration cycle. Measured and simulated beam losses versus time are shown in Figure 21 below. The synchrotron operates with loss levels $\sim 3\%$ over the first 3 ms of the cycle, simulation predicts $\sim 6\%$. Whilst simulation results are high they have good temporal agreement. Beam phase space distributions at 0 ms are shown in Figure 22. Measured longitudinal profiles shown in the bottom right plot in orange show good agreement to simulation. Tomographic longitudinal phase space reconstructions from measured profiles are shown in Figure 23 and are in good agreement with simulation

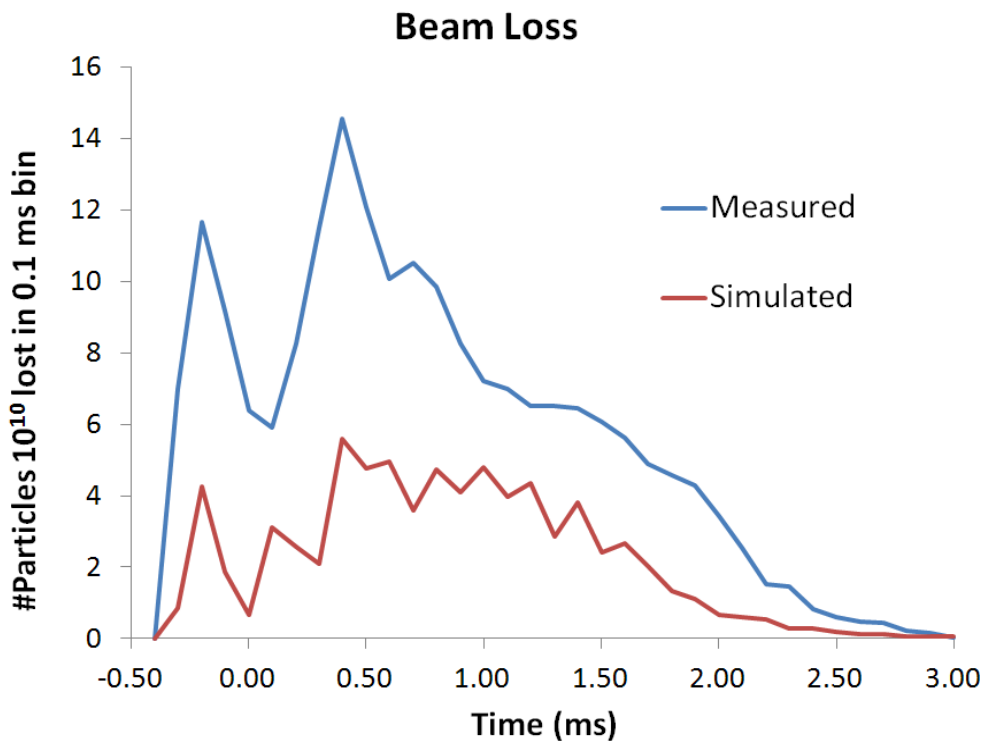


Figure 21: Measured and simulation synchrotron beam loss.

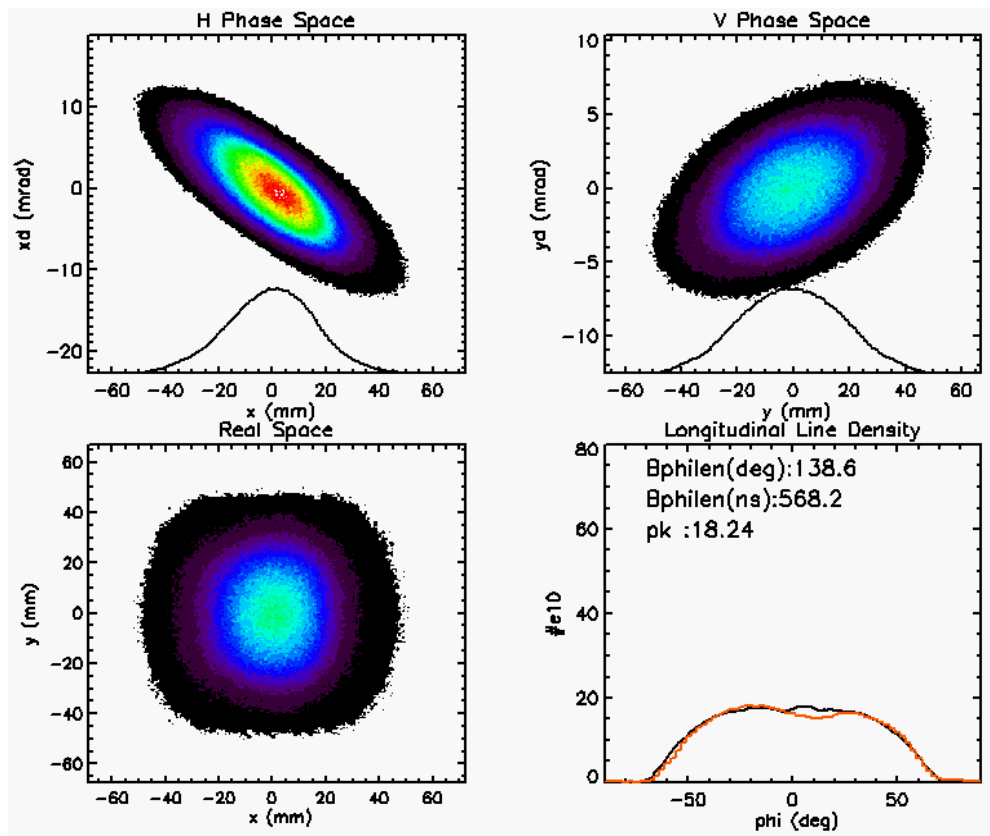


Figure 22: Simulated distributions at 0 ms.

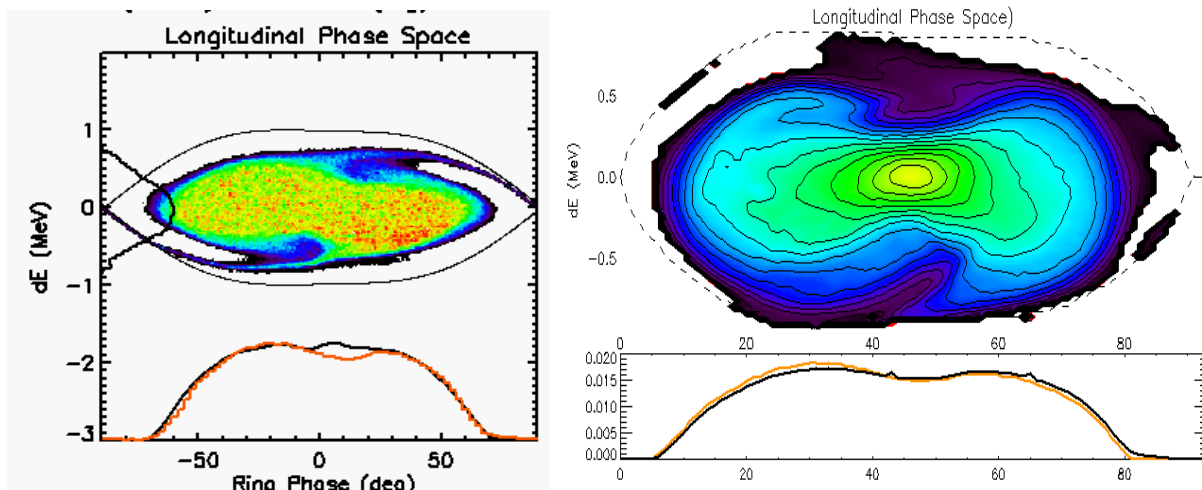


Figure 23: Simulated longitudinal phase space and measured profile at 0ms (left). Tomographic phase space reconstruction (right).

3.10 David S.D. Gunn, Ilian T. Todorov, John A. Purton (CSED)

3.10.1 Defect Formation and Oxygen Vacancy Migration in $Gd_2Ti_2O_7$ and $Gd_2Zr_2O_7$ Pyrochlores

The disposal and safe storage of nuclear waste is a significant challenge for the global community. Several of the radionuclides generated through the nuclear fuel cycle, such as ^{239}Pu and ^{235}U , have long half lives (24,100 years and 7×10^8 years respectively) and careful choice of suitable immobilisation matrices is crucial to prevent any environmental contamination. Such an immobilisation material must be able to withstand prolonged heavy ion particle bombardment while maintaining structural integrity. Pyrochlore-type compounds (see Figure 24) have been proposed as suitable host matrices for this purpose, and great attention has been paid to members of the series $Gd_2(\text{Zr}_x\text{Ti}_{2-x})\text{O}_7$ ($0 \leq x \leq 2$). The radiation tolerance of this series increases with increasing zirconium content, and the healing process in the zirconate is expected to be faster than for the titanate as it does not undergo an amorphous transition upon radiation damage and is a fast ion conductor.

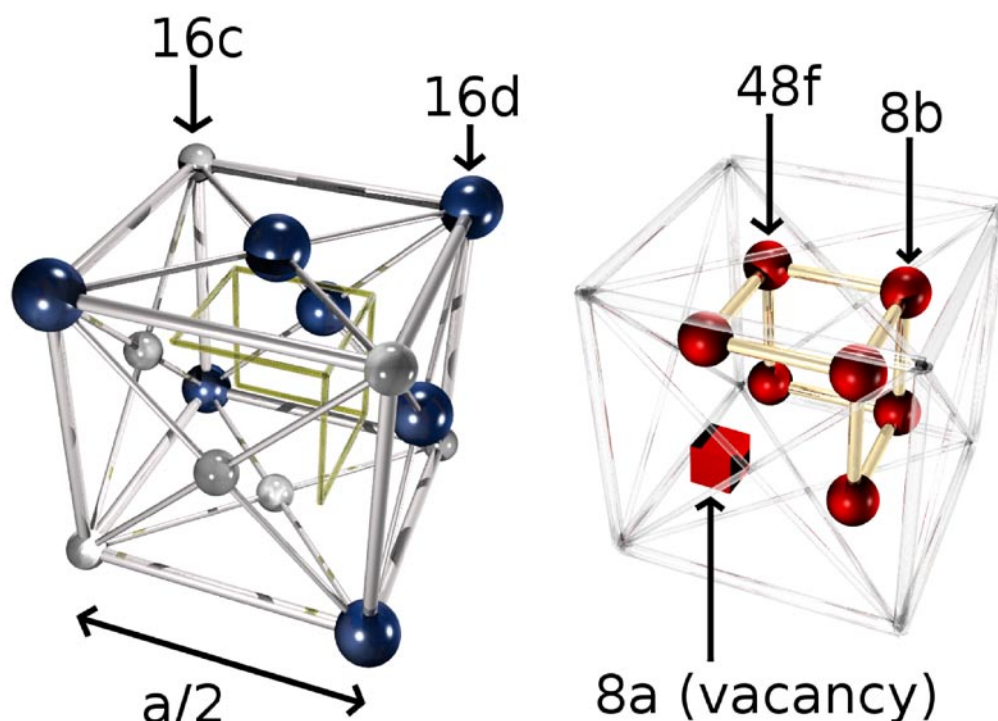


Figure 24: Schematic of one-eighth of the unit cell of a pyrochlore structure ($Fd3m$ symmetry). The cation (left) and anion (right) sublattices are separated for clarity. Gd^{3+} ions are in blue, Ti/Zr^{4+} ions are in silver and O^{2-} are in red.

We have developed a new set of Buckingham potentials, specifically tailored for looking at this $Gd_2(\text{Zr}_x\text{Ti}_{2-x})\text{O}_7$ series. Our research is focussed on calculating defect formation energies and oxygen vacancy migration activation energies so that a clear fundamental understanding of the process of damage formation and healing is obtained.

We have performed equivalent *ab initio* calculations using the ABINIT code to provide further comparison for our atomistic work. We have successfully calculated physical properties, Frenkel pair defect energies and cation antisite defect energies consistent with our atomistic calculations, experimental values and those in the literature.

3.11 C. W. Yong (CSED) and R. Strange (Molecular Biophysics Group, Faculty of Health and Life Sciences, University of Liverpool)

3.11.1 *Computational Studies of motor neuron disease mutants of Cu,Zn superoxide dismutase (SOD1) - insight into mechanisms of toxicity.*

Amyotrophic lateral sclerosis (ALS) is a fatal human neurodegenerative disorder. Mutation of the gene encoding Cu/Zn superoxide dismutase-1 (SOD1) is linked to a subset of familial ALS (fALS). SOD1 mutations decrease protein stability and promote aggregation, both in vitro and in vivo.

Previously, we have simulated long time-scale MD simulations on Scarf machines and demonstrated how molecular dynamics (MD) simulations and small-angle X-ray scatterings (SAXS) can be used together to examine protein conformational states in solution [1]. We are extending our studies to investigate a particular mutant SOD1 species that is known to give aggressive progression of FALS disease, namely, the structure of monomeric copper-apo, zinc-holo fALS mutant A4V SOD1.

The simulation models were set up using DL_FIELD [2], while simulations were run on Scarf machines up to 64 nodes using DLPOLY_4 program [3].

Initial MD results are consistent with un-tethering of the electrostatic (substrate guidance) loop from the main monomer beta-barrel. Dimeric A4V has previously been shown to spontaneously form high molecular weight species in vitro and this work suggests that monomeric apo-A4V is similarly prone. This evidence can be linked with other experimental observations that show that, at physiologically relevant concentrations, the monomeric aggregates are formed directly, bypassing re-attainment of the monomer-dimer equilibrium.

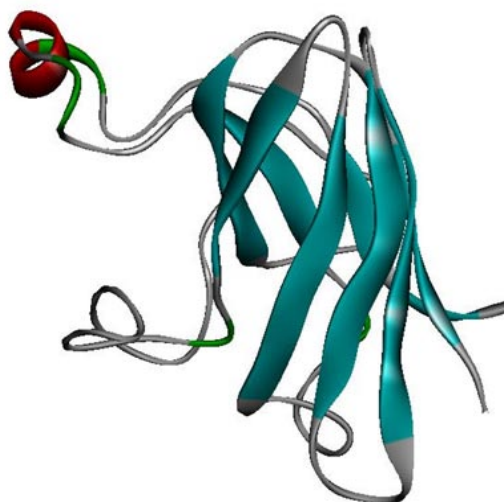


Figure 25: MD simulation snap shot of monomeric copper-apo, zinc-holo fALS mutant A4V SOD1. Notice the uncoil and extension of the electrostatic loop (consists of red alpha helix) as a result of Cu demetallation.

- | |
|--|
| <p>[1] C W Yong, et al. 'Assessment of long-term molecular dynamics calculations with experimental information on protein shape from x-ray scattering-SOD1 as a case study' Chem. Phys. Lett. 481:112-116 (2009).</p> <p>[2] C W Yong, 'DL_FIELD - A force field and model development tool for DL_POLY', R Blake, Ed., CSE Frontier, STFC Computational Science and Engineering, Daresbury Laboratory, p38-40 (2010)</p> <p>[3] I.T. Todorov, W. Smith, K. Trachenko & M.T. Dove, J. Mater. Chem., 16, 1911-1918 (2006)</p> |
|--|

3.12 A.P.L.Robinson, Plasma Physics Group, (CLF)

3.12.1 Ultra-intense lasers

Ultra-intense lasers have a number of potential applications with transformative capability. Two that are particularly interesting are the possibility of generating high energy ion beams (perhaps even for medical applications) and generating intense relativistic electrons beams in dense plasmas that can ignite compressed DT fuel for inertial fusion energy production.

Both research areas have been pursued in this period using numerical simulations that we carried out on the SCARF-LEXICON cluster. In terms of proton acceleration we used large 2D particle-in-cell simulations to further investigate an idea we had started developing in the previous year. The idea centred around an obstacle to improving the energies that hole-boring radiation pressure acceleration (HB-RPA) can reach. In HB-RPA an ion beam is generated as a laser pulse ploughs into a block of plasma and the raw radiation pressure of the laser pulse rapidly accelerated ions at the irradiated surface. It was thought that high plasma densities would be needed to ensure that the laser pulse would not enter the plasma, which in turn would limit the achievable energy. In our recent publication [2] we showed that non-linear effects overcome this problem, even in a 2D scenario, which means that energies 3-4 times higher than expected might be realizable.

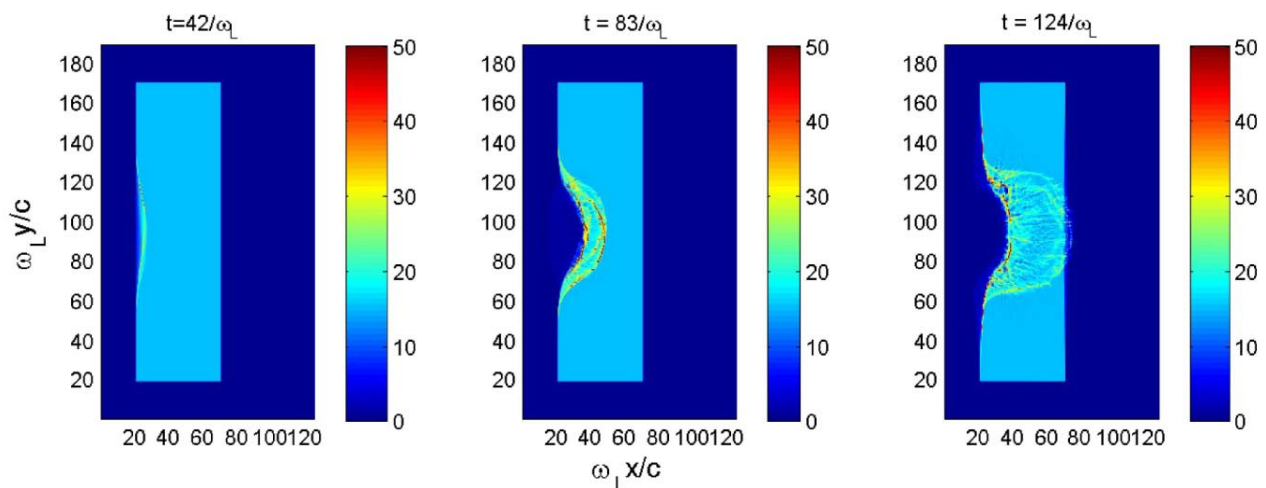


Figure 26: Ion Density Plots during Hole-Boring RPA generated in 2D PIC simulation performed on SCARF-LEXICON-2

We have also continued to develop the resistive guiding concept for Fast Ignition ICF. The development work done throughout 2011 resulted in our work appearing in Physical Review Letters [1]. We have continued to use the SCARF-LEXICON clusters to continue our research into resistive guiding throughout 2012.

We have also recently been awarded an European Research Council Starting Grant (STRUCMAGFAST) to support the development of resistive or structured guiding research at the CLF over the next four years. This will include the development of a new parallel simulation code, and a post-doctoral researcher.

The SCARF resources have been invaluable in providing support to the CLF user community through our support role. We have provided support through performing simulations for CLF users, developing codes for CLF users to use on SCARF, and training students to use these codes on the SCARF resources.

[1] A.P.L.Robinson, M.H.Key and M.Tabak, Phys.Rev.Lett, 108, 125004 (2012)

[2] A.P.L.Robinson, R.Trines, Z.Najmudin, and N.Dover, Plasma Phys.Control. Fusion, 54, 115001 (2012)

3.13 Bin Qiao (QUB), Macro Borghesi (QUB), Matthew Zepf (QUB), David Neely (RAL)

3.13.1 Scarf usage summary of Queens University Belfast plasma physics in 2012

In the past year, Queen's University Belfast (QUB) plasma physics group has carried out comprehensive particle-in-cell (PIC) modelling work on the SCARF cluster at Rutherford Appleton Laboratory in the area of laser-driven high-energy ion sources production. These modelling results have helped the group to understand the new ion acceleration mechanism, specifically radiation pressure acceleration (RPA), to explain the group's experimental results on Vulcan and Gemini laser facilities. The PIC code "ILLUMINATION" of this group has also been benchmarked and improved in comparison with the experimental data.

In Summary:

3.13.1.1 Proposing the new hybrid light-sail (LS) - target normal sheath acceleration (TNSA) regime for ion acceleration by linearly polarized laser pulses at intensities of 10^{21}Wcm^{-2}

Through a large number of 2D PIC simulations on the SCARF-INTEL and theoretical modeling, we have identified a new RPA-dominated regime of quasimonoenergetic ion beam generation for LP laser pulses at intensities of 10^{20} – 10^{21}Wcm^{-2} . In this regime, with an appropriate coupling condition between foil thickness, laser intensity, and pulse duration satisfied, RPA could be dominant during the competition between RPA and TNSA mechanisms in a hybrid acceleration stage. Such a coupling condition has been analytically derived and verified by two-dimensional (2D) particle-in-cell (PIC) simulations. These show that 1.26 GeV quasimonoenergetic C⁶⁺ ion beam with energy spread $\sim 0.1 \text{GeV}$ and angular divergence $< 5^\circ$ is obtained by irradiation of 80 nm ultrathin foils with LP pulses at intensities 10^{21}Wcm^{-2} . The result is shown in following Fig. 1. We can see that the RPA dominated regime can be achieved by using ultrathin foils (tens of nanometers) on contemporary high-contrast petawatt or subpetawatt laser systems. Furthermore, a laser contrast in excess of 1010 is required for the regime; otherwise, the prepulse heating will lead to rapid foil disassembly. This theoretical and numerical work opens the proper way to verify the RPA scheme in experiments with optimized laser and target parameters, and has been published in Physical Review Letters [1].

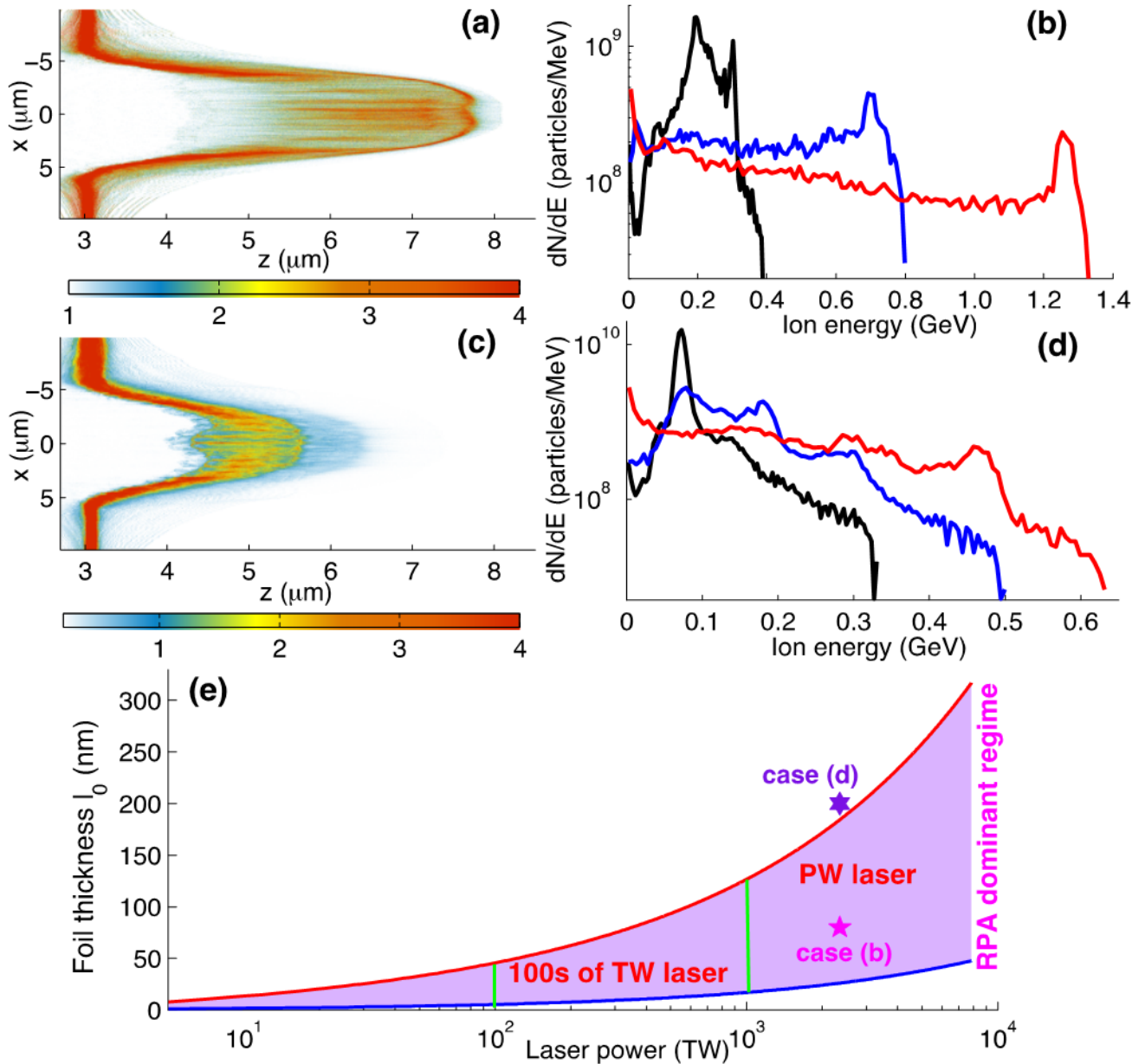


Figure 27: (a) C6+ density at $t=83\text{fs}$ for a 80nm fully ionized carbon foil irradiated by LP laser pulses at intensities $I_0=3\times 10^{21}\text{ Wcm}^{-2}$, wavelength $\lambda=1.0\mu\text{m}$ and duration $\tau_L=67\text{ fs}$, where the foil electron density is 600nc. (b) The corresponding C6+ energy spectra at $t=53$ (black line), 68 (blue line), and 83fs (red line), showing RPA dominated regime in hybrid RPA-TNSA acceleration. (c) and (d) C6+ density and spectra obtained by increasing foil thickness to $I_0=200\text{nm}$, showing no pronounced spectral peak as RPA is non-dominated in the hybrid acceleration. (e) shows the scaling of the required foil thickness for the RPA-dominated regime with the laser power by fixing laser pulse duration at 66 fs, where the foil density is the same as in Figure 27(a). The corresponding points of the spectral cases of (b) and (d) are also marked in (e).

3.13.1.2 Scaling study of RPA with both experiments on Vulcan laser and PIC simulations

The extensive PIC simulations on SCARF cluster we have carried out have explained and supported our recent excellent experimental results on the PW Vulcan laser facility, which shows clear evidence of RPA narrow band spectral features emerging from ultrathin foil irradiation by sub-PW laser pulses, as seen in Figure 28.

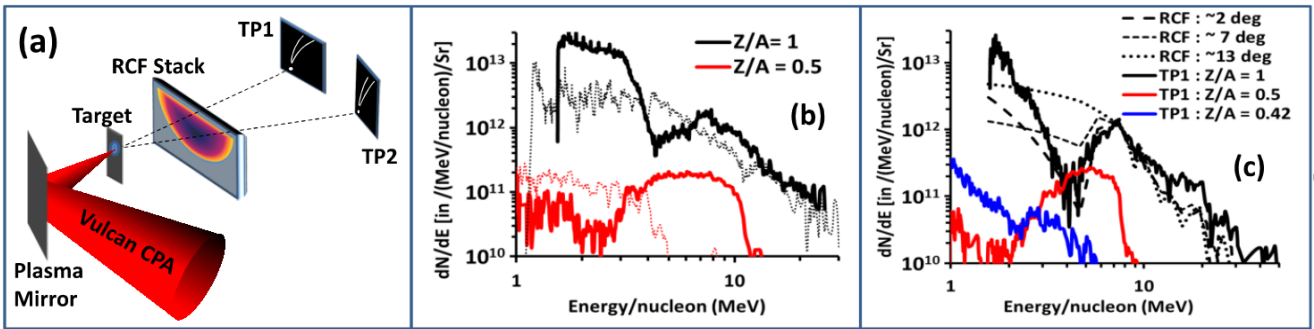


Figure 28: (a) Schematic of the experimental setup. (b) Ion spectra obtained from 100 nm Cu target irradiated by a LP laser pulse at $I_0 \sim 3 \times 10^{20} \text{ W cm}^{-2}$. Different line colours correspond to different ion species (see the figure legend), solid and dotted lines represent spectra obtained on TP1 and TP2 respectively. (c) Ion spectra obtained on TP1 from 50 nm Cu target irradiated by a CP pulse at $I_0 \sim 1.25 \times 10^{20} \text{ W cm}^{-2}$. The proton spectra obtained with RCF, in the same shot, at different positions in the beam, corresponding to $\sim 2^\circ$, $\sim 7^\circ$ and $\sim 13^\circ$ from the laser axis are also shown (dashed lines).

In particular, carbon ion peaks of up to $\sim 7 \text{ MeV/nucleon}$ (cut-off energy in excess of 10 MeV/nucleon) are produced for the first time, with nearly an order of magnitude higher particle flux than previously reported. The PIC simulation result in Figure 29 show that TNSA and HB takes place with the rising intensity of the laser pulse, accelerating ions from rear and front surfaces respectively. After the ions from the front surface pile up at the target rear surface forming a compressed layer, ions are accelerated predominantly by the LS mechanism resulting in the ion spectrum shown in the Figure 29(c), which reproduces the main features observed in the experimental data. The target remains highly reflective during the whole duration of the simulation and the carbon ions are accelerated in a snowplough fashion maintaining a dense layer as shown in the Figure 29(d) and (e). It is interesting to note the debunching of the Cu ions after the laser pulse, as shown in the Figure 29(e), producing the exponential spectrum profile of Figure 29(c), which resembles closely the experimental data.

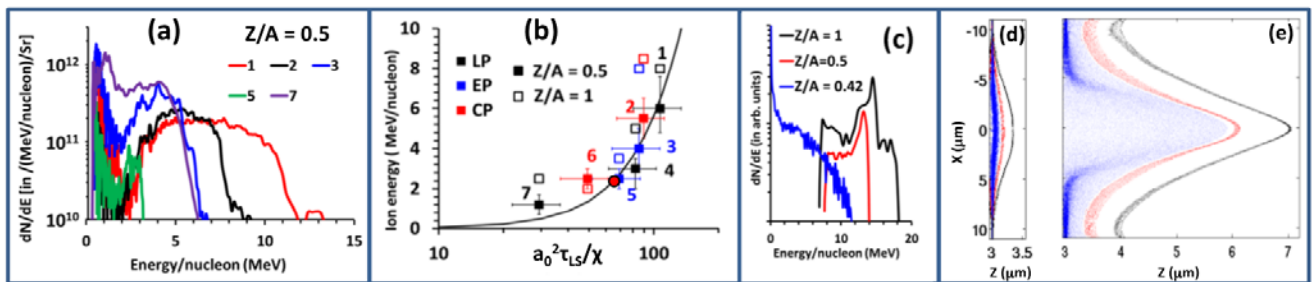


Figure 29: (a) Graph showing comparison between five ion ($Z/A = 0.5$) spectra, where the spectral peaks are plotted in (b) as a function of $a_0^2\tau_{LS}/\chi$. The experimental parameter set [a_0 , target material, target thickness(μm)] for the data points 1-7 are [15.5, Cu, 0.1], [10, Cu, 0.05], [13.8, Cu, 0.1], [7.5, Al, 0.1], [6.9, Al, 0.1], [13.6, Al, 0.5] and [14.1, Al, 0.8] respectively. The black solid line in (b) represents ion energy estimated from the analytical modeling described in the text. The red circles represent the data shown by Heing et. al. in the ref. [16]. (c) Ion spectra obtained from 2D multilayered PIC simulation for the data point '1' in (a), of which the experimental spectra is shown in the Figure 27(b). (d) and (e) shows 2D profiles of ion (black-proton, red-carbon and blue-Copper) density obtained from the 2D PIC simulation shown in (c) at 66 fs and 165 fs, respectively.

where the heavier species in a multispecies target undergo decompression and Coulomb explosion, while the lighter species are stabilized by the excess electrons released by the heavier species.

The scaling with the laser and target parameters, point to a multispecies scenario of LS RPA acceleration is also given by numerous simulations in comparison with experimental data, shown in Figure 30. The possibility of achieving spectral peaks beyond 100 MeV/nucleon, a key requirement for hadron therapy, by tuning currently achievable laser and target parameters is discussed on the basis of the experimental scaling, and also verified by 2D PIC simulations.

These results have been accepted by Physical Review Letters [2].

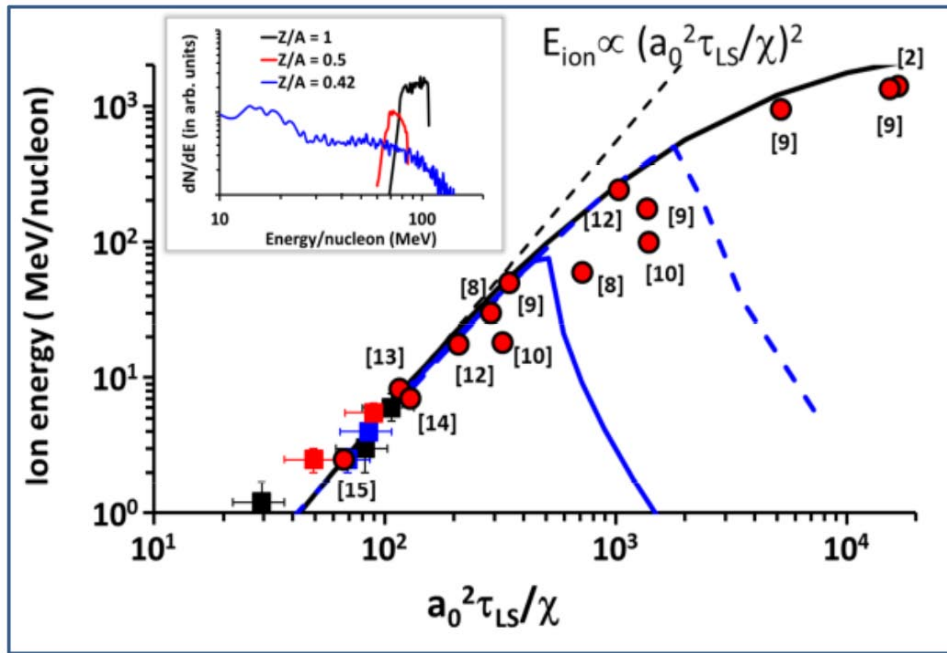


Figure 30: Ion energy scaling (black solid line) as shown in the Figure 29(a), extrapolated to higher $a_0^2\tau_{LS}/\chi$. Square points are the experimental data. The red circles represent the results reported in the literature, by multispecies PIC simulations for stable LS acceleration. Dashed black line shows trend for a $E_{ion} \propto (a^2\tau_{LS}/\chi)^2$ scaling valid for ion energies. Solid and dashed blue lines plots expected ion energy by varying χ for 45 fs FWHM laser at $I_0 = 5 \times 10^{20} \text{ W cm}^{-2}$ and 450fs FWHM laser at $I_0 = 5 \times 10^{19} \text{ W cm}^{-2}$ respectively. The insert shows the spectra obtained from a PIC simulation identical to the run shown in the Figure 29 (c), except the laser fluence increased by a factor of 2 and target density decreased by a factor of 2.5.

[1] B. Qiao et al Phys. Rev. Lett. 108, 115002 (2012).
 [2] S. Kar, K.F. Kakolee, and B. Qiao et al., Phys. Rev. Lett. Accepted (2012)

3.14 Rowan Hargreaves (ISIS)

3.14.1 *Measuring the effect of temperature on micelle structure using wide Q-range neutron diffraction*

Using wide Q-range neutron diffraction and Empirical Potential Structure Refinement (EPSR) we have been able to determine the effect of a 25 degree increase in temperature on the structure of C10TAB micelles in solution. We observe at the higher temperature that there is a far greater range of micelle sizes and that the micelles are more disordered with greater eccentricity and a less precisely defined interface between the hydrophobic core and outer corona than at ambient conditions. These are marked structural changes that are occurring as a result of a modest change in temperature.

The idea of self assembly is a simple one: an amphiphilic molecule will aggregate to shield their solvophobic parts from the solvent with their solvophilic moieties forming an interface to the solvent. Depending upon the concentration, the size and shape of the amphiphilic molecule a variety of different aggregates can form: spherical or elliptical micelles, rod-like micelles and more complicated bi-layer structures including vesicles and lamellae.

In the 1970s Tanford[1], Mitchell, Ninham and Israelachvili [2] developed a simple thermodynamic model to predict the morphology of structures that surfactants form in solution. These models distilled a single parameter, known as the packing parameter, that governed the size and shape of the aggregate formed. The packing parameter is a function of the average surfactant hydrophobic tail length and volume, and the area per surfactant molecule of the interface formed between the hydrophobic region and polar region of the aggregate. (NB while the tail length and volume are geometric properties, the interface area is in fact a free energy.) Unfortunately to capture all the subtleties of the different phenomena of surfactant self-assembly the model has increased in complexity.

The experimental technique wide Q-range neutron diffraction is able to interrogate the structure of liquid and disordered materials on length scales from the atomistic to the mesoscopic. This is in direct contrast with most other experimental techniques that either provide an indirect or range limited measurement of the micelle structure. Unfortunately the direct interpretation of the raw neutron diffraction data is, with exception of the simplest systems, very difficult or nigh on impossible.

We are able to interpret the diffraction data by the computer simulation technique EPSR, that refines 3d configurations of the molecules towards ones that are as consistent, as can be, with the measured diffraction data. Starting from an initial random configuration of molecules EPSR assembles the surfactant molecules into micelles, as expected. We now have a wealth of information about the micelles – everything from the atomistic detail of surface of the micelle (the counterion binding and water penetration) to the size and shape of the micelle itself.

Building on our previous study [3], our recent work has shown that we are able to see marked differences in the micelles formed at the two temperatures of 25C and 50C. Figure 31 is an example of the sort of structural detail we able to extract from our models, it shows the atomic density profiles (ADPs) of various atom types from the centre of mass of the micelles found at the two temperatures revealing the difference in the cross-sectional structure of the micelles. From this it is

clear that the interface between the hydrophobic part of the micelle and the outer polar region is less well defined at the higher temperature of 50C than at 25C. The ADPs corresponding to the surfactant headgroups and counterions are significantly broader at 50C than at 25C reflect the increased disorder at the higher temperature.

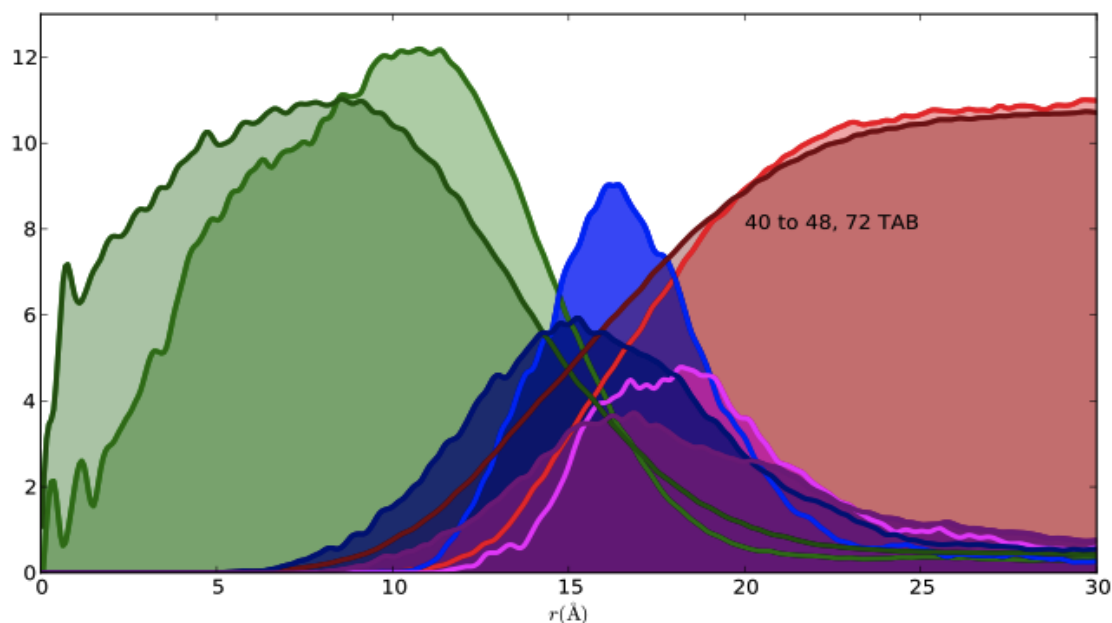


Figure 31: A comparison of the atomic density profiles (ADPs) calculated from the centre of mass of micelles containing between 40 and 48 surfactant molecules measured at 25C (lighter lines) and 50C (darker lines). The green lines correspond to the carbon atoms in the surfactant molecules' hydrophobic tail, and the blue lines correspond to the nitrogen atoms in the surfactants' headgroups. While the magenta/purple lines show the location of the bromide counterions and the red lines are the water molecule locations (NB the water ADPs have been scaled up by a factor of 10 for clarity).

The combination of wide Q-range neutron diffraction and EPSR is able to provide the molecular-level detail that is vital to understand self-assembly processes and more generally these sorts of systems where the large scale structure is governed by molecular-level interactions. For example, different counterions can produce radically different aggregates but what exactly is the mechanism – and where do the different counterions sit in relation to the aggregate? Insights from these sorts of study are of particular importance to the field of supramolecular templating--a method of forming nanostructured materials by using molecular aggregates, like micelles, as scaffold to form the material around – which is used to manufacture molecular sieves and catalysts.

This sort of study would not be possible without the use of SCARF. Having access to the many cores on SCARF has allowed us to experiment with different models to improve the refinement process, to run multiple simulations of the same model to gain sufficient statistics and to concurrently run simulations using data from different neutron experiments for comparison. For some perspective, at present--due to EPSR currently being a serial code--8 months of CPU time is required for the analysis of one day of beam time!

[1] Tanford C, *The Hydrophobic Effect*; Wiley-Interscience. New York, 1973.

[2] Israelachvili J, Mitchell D J, and Ninham B W; *J. Chem. Soc., Faraday Trans. 2*, 1976, 72, 1525.

[3] Hargreaves R, Bowron D T, and Edler K; *J. Am. Chem. Soc.* 2011, 133, 16524-16536

3.15 E. Higson^{1,2}, R. Trines², R. Bingham^{2,3}, and P.A. Norreys^{1,2,4} [1]University of Oxford [2] Central Laser Facility, [3] University of Strathclyde, [4] Imperial College London.

3.15.1 *The role of phase front deformation on the growth of the filamentation instability in laser-plasma interactions*

The filamentation instability plays an important role in the interaction of intense laser pulses with dense plasma or with solid targets. It can have a detrimental effect on processes ranging from channel formation in underdense plasma to target compression in Inertial Confinement Fusion prior to ignition. Previous results indicated that phase front deformation caused by transverse density fluctuations across the laser spot were an important factor in determining the onset and extent of laser pulse filamentation for plasma densities just below the critical density. In this paper, the role of such phase front deformation will be explored further.

In this paper, particle-in-cell simulations are presented in which a low-intensity laser pulse propagates through a plasma with a prescribed density profile (a channel), obtained from two-dimensional particle-in-cell simulations of hole boring by relativistic laser beams. This way, the influence of the plasma density profile on the laser beam and its phase fronts can be studied while the laser beam is too weak to alter the density profile significantly. The following function was used to reproduce the charge density spatial profile (shown in Figure 32):

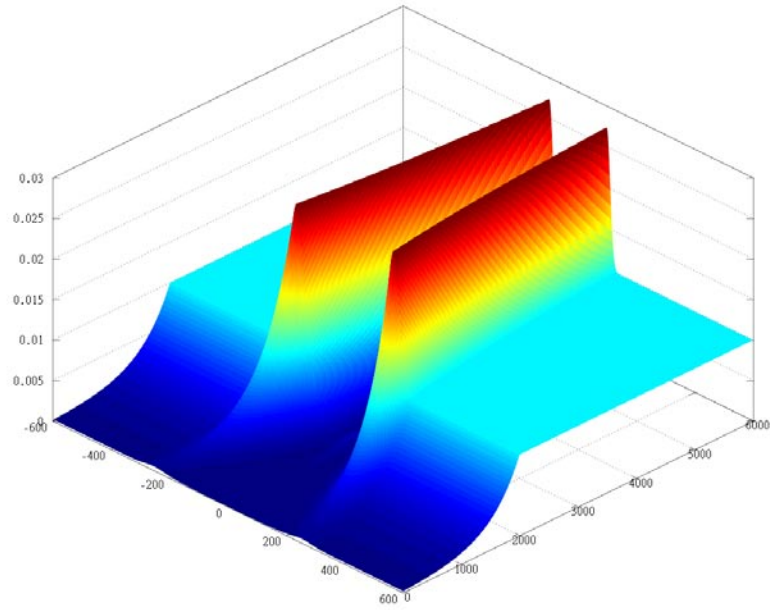
$$f(x,y)=(3.75 \times 10^{-3} u^{16} - 9.5 \times 10^{-3}) \exp(-u^4) + 0.01 + 4.0 \times 10^{-3} (\exp(-64u^2))$$

$$\text{where } x_1 = \frac{35000x}{2\pi \times 10^6} \quad y_1 = \frac{3333y}{2\pi \times 10^6} \quad u = x_1 \left(1 + \frac{y_1}{2}\right)$$

When modelling of exponential ramp (as in Figure 32) was required, $f(x,y)$ was multiplied by a ramp factor for y less than the length of the ramp (L_{ramp}).

$$\text{ramp} = \exp\left[\frac{8(y - L_{\text{ramp}})}{L_{\text{ramp}}}\right]$$

(a)



(b)

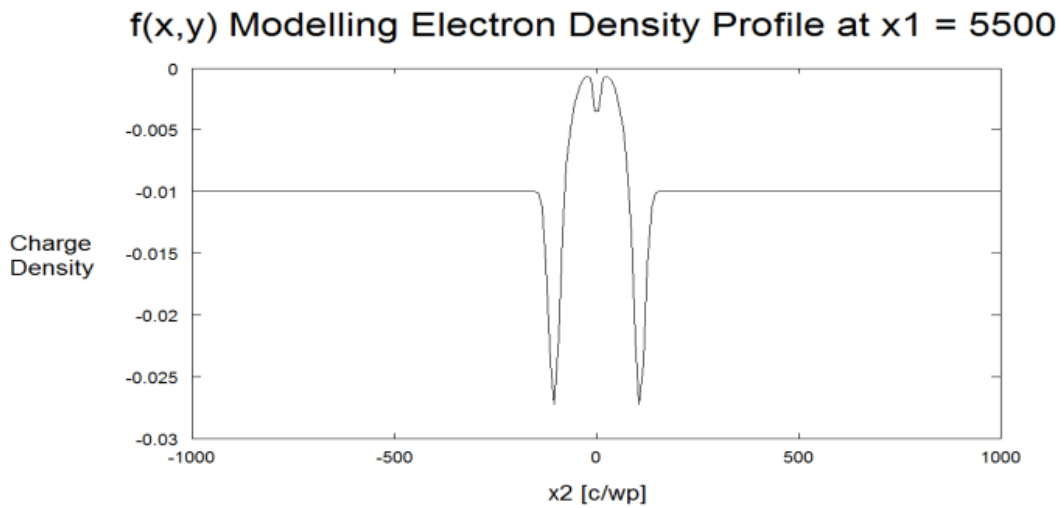


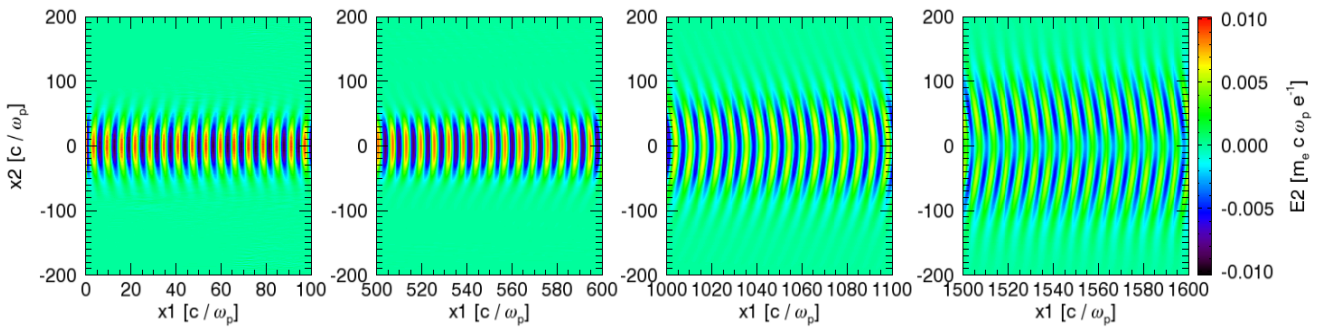
Figure 32: (a) Colour plots of $f(x,y)$ (b) Transverse line-out of the function under (a) at $x_1 = 5500$.

The 2D PIC simulation results depicted in Figure 33c and Figure 33d have been obtained using the PIC code OSIRIS [31]. The simulation setup was the same as for Figure 32. As shown in Figure 32 and Figure 33, a plasma channel is then formed with steep walls (2–2.5 times the background density n_b) and a low density near its axis (0.1–0.2 times n_b). The channel in the quasi-static model closely follows the shape of the channel in the PIC simulations.

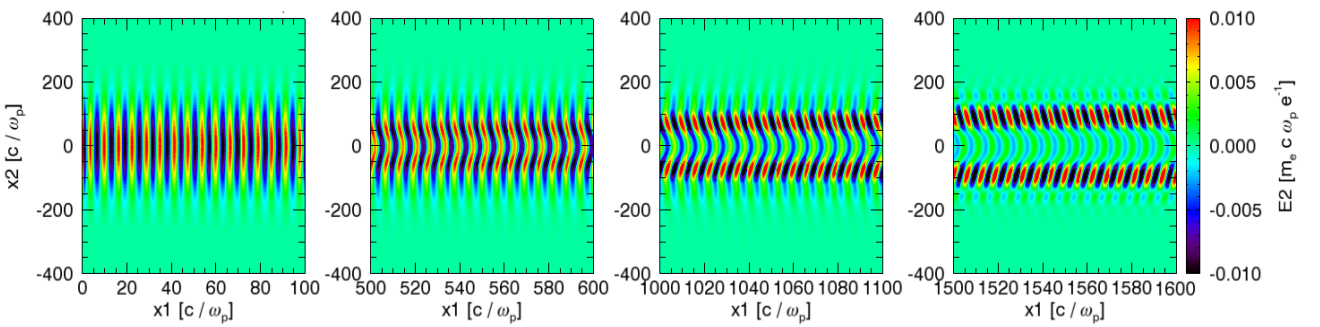
In order to verify the predictions of the quasi-static model, a sequence of PIC simulations has been carried out. The simulations have been carried out on the CLF-owned Scarf-Lexicon cluster, using the particle-in-cell code Osiris. In the simulations, a reduced laser intensity of $1.3 \times 10^{18} \text{ W cm}^{-2}$ was used, corresponding to $a_0 = 0.01$. This intensity is sufficiently low for the laser pulse not to significantly perturb the plasma, while the effect of the plasma density profile on laser pulse propagation is faithfully preserved. Numerical parameters of these simulations were as follows: box dimensions: 7825×3016 (in units of c/ω_p); the time at which the snapshots were taken 7519 (in units of ω_p^{-1}).

Figure 33(a) shows the electric field at different times in the simulation, providing information individual wave-fronts, plasma density profiles given by equation (1). Shown in Figure 33(b) is its transformation where the plasma density is doubled but its gradient with respect to the transverse direction is kept constant [$2f^{1/2}(x,y)$]. One can clearly see that the greater phase discrepancy between wave-fronts, caused by a greater plasma density, causes the beam to bifurcate much faster. This also causes the beamlets to be more focused and intense, as shown by the red colours of the wave fronts. Figure 33(c) shows a transformation that shrinks the transverse axis by a factor of two, increasing the transverse spatial gradient of phase change but keeping the other factors constant [$f(2x,y)$]. This requires consideration of the competition between increased self-focusing and the effect of the larger gradient. Comparison of Figure 33(a) and Figure 33(c) provides compelling evidence that the larger gradient does indeed cause the beam to bifurcate faster. If this were not the case, then the increase in self-focusing would mean that the beam would split much more slowly. Hence this demonstrates that the larger gradient of phase change increases the bifurcation speed.

(a) Plasma Density Profile = $f(x, y)$



(b) Plasma Density Profile = $2[f(\frac{x}{2}, y)]$



(c) Plasma Density Profile = $f(2x, y)$

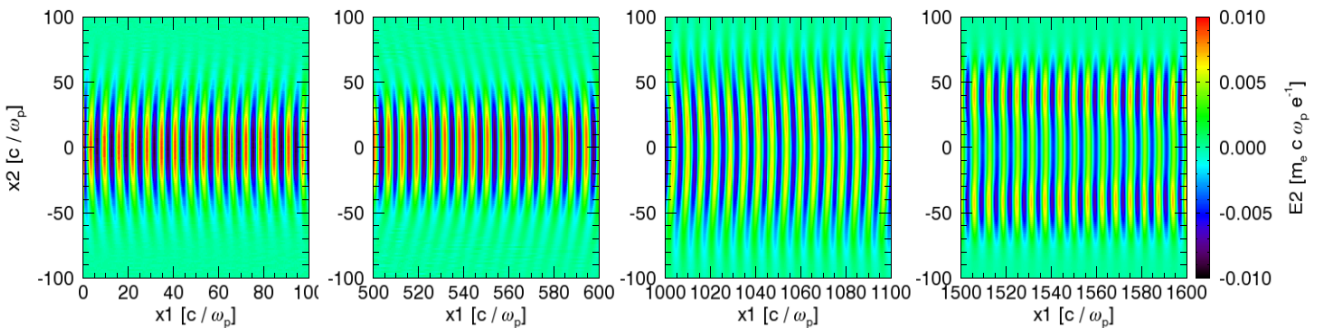


Figure 33: Effect of absolute plasma density and density gradient on laser beam propagation. (a) Propagation in the standard channel given by $f(x,y)$. (b) Propagation in the modified channel $2f(x/2,y)$, so the amplitude of the density perturbation is doubled while the density gradients are preserved. (c) Propagation in the modified channel $f(2x,y)$, so the density gradients are doubled while the amplitude of the density perturbation is preserved.

In conclusion, we have studied the influence of the transverse plasma profile on laser beam filamentation. It was found that this is strongly dependent on the width of the channel and the steepness of the channel walls. In the future, this may be used to control the onset of filamentation via the laser pulse spot diameter.

1. APPENDIX : SCARF HARDWARE DETAILS

Host group	CPU type and frequency	Nodes	Cores /node	Total cores	Interconnect	Total memory
SCARF12	Intel X5675 @ 3.06GHz	20	12	240	QDR Infiniband	960GB
SCARF11	Intel X5660 @ 2.8GHz	32	12	384	QDR Infiniband	768GB
Lexicon-2/ SCARF10	Intel E5530 @ 2.40GHz	104	8	832	DDR Infiniband	2496 GB
IBIS/ SCARF09	Intel E5462 @ 2.80GHz	48	8	384	SDR Infiniband	768 GB
SCARF08	Intel E5430 @ 2.66GHz	46	8	368	SDR Infiniband	736 GB
Lexicon/ SCARF07	AMD Opteron 275 @ 2.2GHz	73	4	292	GB Ethernet	584 GB
General/ SCARF06	AMD Opteron 285 @ 2.6GHz	50	4	200	Myrinet	400 GB
Grand Totals		373		2700		6712GB

2. APPENDIX: INDEX OF FIGURES

Figure 1: Pie chart showing percentage usage of the SCARF service by department4

Figure 2: Table displaying detailed usage from 2011-12 comparing with 2010-11 and 2009-105

Figure 3: Availability for SCARF6

Figure 4: Availability vs Year Purchased6

Figure 5: Scheme of the C5 species present over a working Pd/Al2O3 hydrogenation catalyst utilizing a mixed *cis*- and *trans*-1,3-pentadiene feedstock that contains cyclopentene as an impurity. Gas-phase species are denoted by (g) and adsorbed species by (ad). Assignment of the vibrational spectra of the molecules highlighted in red were provided by Gaussian 03 calculations on SCARF.9

Figure 6: Left: the CASTEP geometry optimised structure of 2,2'-bipyridyl (bis)thiolate platinum (II), Pt(bpy)(SPh)₂ calculated on SCARF. Right: Comparison of the INS spectrum of the complex generated from the structure shown on the left (blue trace) with that measured on TOSCA at ISIS (red trace).....10

Figure 7: Adsorption of CO₂ in siliceous MFI at 308K, comparing experiment¹ to simulation.....11

Figure 8: {011} siliceous FAU slab filled with CO₂ (top). Diffusion density profile of CO₂ in this slab (bottom), where red represents the favoured adsorption sites.....12

Figure 9: Interaction of energetic particles with a magnetohydrodynamic (MHD) background plasma: (a) Background thermal pressure with a shock advancing from the right (b) energy density of energetic particles showing that some particles escape ahead of the shock and generate a magnetic field that confines other particles at the shock (c) magnitude of the magnetic field excited by streaming energetic particles. The panels to the right display the same information in a different format. (d-f) show the structure of the magnetic field perpendicular to the direction of particle streaming.....14

Figure 10: The Diamond beam before propagating through the plasma cell (top), after the plasma cell where microbunches are visible (middle) and the wakefield that has microbunched the beam (bottom).....15

Figure 11: Adsorption energies of hydrogen on graphene and a single-layer of *h*-BN. Each histogram refers to a different configuration of the molecule on the substrate. The solid part of the histograms refers to the results obtained with the optB88-vdW functional, while the bottom part refers to the PBE results.16

Figure 12: The solid lines refer to the interlayer binding curves of graphite and *h*-BN. The dashed curves refer to the interlayer binding of the two materials when a hydrogen molecule is absorbed between the layers. The dashed curves clearly highlight the expansion of the interlayer spacing of the two materials due to the absorption of the gas molecule and a subsequent decrease of the binding energy.....17

Figure 13: The dashed curves represent the absorption energy per hydrogen molecule as a function of interlayer spacing in graphite and *h*-BN, where the interlayer distance is ~3.33 Å. The solid lines refer to the absorption energy per hydrogen molecule in the pre-expanded materials.....18

Figure 14: Evolution of longitudinal profile (mountain range) as a function of time with colour indicating particle population, for approximate ISIS parameters.19

Figure 15: Longitudinal phase space (top) at the end of injection (0 ms), mid-cycle (5 ms) and just prior to extraction (10 ms) for approximate ISIS running parameters. Momentum spread, bunching factor and stability parameters (bottom) as a function of time through 10 ms cycle for approximate ISIS parameters.20

Figure 16: Spin densities on the 110 plane of the (a) intrinsic Si (b) p-type Si, (c) n-type Si host for the range of -0.02μB /bohr³ to 0.02μB/bohr³ with a step of 2x10⁻⁴ μB /bohr³. The blue lines are for majority spin states and red lines are for minority spin states. The

highest magnitude of spins for each type of spin is at the centre of contours. (d) The long range spin polarisation of the p-type Si:Mn. The range of this plot is $-0.02 \mu\text{B}/\text{bohr}^3$ to $+0.0002 \mu\text{B}/\text{bohr}^3$. The range has been modified from the former to include atoms having.....21

Figure 17: Rhombohedral structure of LaCoO_3 22

Figure 18: Density functional simulation of IR spectrum of Croconic acid compared with experiment.23

Figure 19: The INS of pH_2 in Fe MOF. Top) pure pH_2 . Bottom) one equivalent load of D_2 and further pH_2 . Demonstrating the existence of two sites for adsorption.[4] SCARF calculations were used to determine the DoS of the empty cage.24

Figure 20: Determination of the absorption site of CO_2 in NOTT 300 using INS and DFT (SCARF calculations)25

Figure 21: Measured and simulation synchrotron beam loss.26

Figure 22: Simulated distributions at 0 ms.....27

Figure 23: Simulated longitudinal phase space and measured profile at 0ms (left). Tomographic phase space reconstruction (right).....27

Figure 24: Schematic of one-eighth of the unit cell of a pyrochlore structure ($\text{Fd}3\text{m}$ symmetry). The cation (left) and anion (right) sublattices are separated for clarity. Gd^{3+} ions are in blue, Ti/Zr^{4+} ions are in silver and O^{2-} are in red.28

Figure 25: MD simulation snap shot of monomeric copper-apo, zinc-holo fALS mutant A4V SOD1. Notice the uncoil and extension of the electrostatic loop (consists of red alpha helix) as a result of Cu demetallation.29

Figure 26: Ion Density Plots during Hole-Boring RPA generated in 2D PIC simulation performed on SCARF-LEXICON-230

Figure 27: (a) C^{6+} density at $t=83\text{fs}$ for a 80nm fully ionized carbon foil irradiated by LP laser pulses at intensities $I_0=3 \times 10^{21} \text{ W cm}^{-2}$, wavelength $\lambda=1.0\mu\text{m}$ and duration $\tau_L=67 \text{ fs}$, where the foil electron density is 600nc. (b) The corresponding C^{6+} energy spectra at $t=53$ (black line), 68 (blue line), and 83fs (red line), showing RPA dominated regime in hybrid RPA-TNSA acceleration. (c) and (d) C^{6+} density and spectra obtained by increasing foil thickness to $l_0=200\text{nm}$, showing no pronounced spectral peak as RPA is non-dominated in the hybrid acceleration. (e) shows the scaling of the required foil thickness for the RPA-dominated regime with the laser power by fixing laser pulse duration at 66 fs, where the foil density is the same as in Figure 27(a). The corresponding points of the spectral cases of (b) and (d) are also marked in (e).32

Figure 28: (a) Schematic of the experimental setup. (b) Ion spectra obtained from 100 nm Cu target irradiated by a LP laser pulse at $I_0 \approx 3 \times 10^{20} \text{ W cm}^{-2}$. Different line colours correspond to different ion species (see the figure legend), solid and dotted lines represent spectra obtained on TP1 and TP2 respectively. (c) Ion spectra obtained on TP1 from 50 nm Cu target irradiated by a CP pulse at $I_0 \approx 1.25 \times 10^{20} \text{ W cm}^{-2}$. The proton spectra obtained with RCF, in the same shot, at different positions in the beam, corresponding to $\sim 2^\circ$, $\sim 7^\circ$ and $\sim 13^\circ$ from the laser axis are also shown (dashed lines).....33

Figure 29: (a) Graph showing comparison between five ion ($Z/A = 0.5$) spectra, where the spectral peaks are plotted in (b) as a function of $a_2\tau_{\text{LS}}/\chi$. The experimental parameter set [a_0 , target material, target thickness(μm)] for the data points 1-7 are [15.5, Cu, 0.1], [10, Cu, 0.05], [13.8, Cu, 0.1], [7.5, Al, 0.1], [6.9, Al, 0.1], [13.6, Al, 0.5] and [14.1, Al, 0.8] respectively. The black solid line in (b) represents ion energy estimated from the analytical modeling described in the text. The red circles represent the data shown by Heing et. al. in the ref. [16]. (c) Ion spectra obtained from 2D multilayered PIC simulation for the data point '1' in (a), of which the experimental spectra is shown in the Figure 27(b). (d) and (e) shows 2D profiles of ion (black-proton, red-carbon and blue-Copper) density obtained from the 2D PIC simulation shown in (c) at 66 fs and 165 fs, respectively.33

Figure 30: Ion energy scaling (black solid line) as shown in the Figure 29(a), extrapolated to higher $a_2\tau_{\text{LS}}/\chi$. Square points are the experimental data. The red circles represent the results reported in the literature, by multispecies PIC simulations for stable LS acceleration. Dashed black line shows trend for a $E_{\text{ion}} \propto (a^2\tau_{\text{LS}}/\chi)^2$ scaling valid for ion energies. Solid and dashed blue lines plots expected ion energy by varying χ for 45 fs FWHM laser at $I_0 = 5 \times 10^{20} \text{ W cm}^{-2}$ and 450fs FWHM laser at $I_0 = 5 \times 10^{19} \text{ W cm}^{-2}$ respectively. The insert shows the spectra obtained from a PIC simulation identical to the run shown in the Figure 29 (c), except the laser fluence increased by a factor of 2 and target density decreased by a factor of 2.5.....34

Figure 31: A comparison of the atomic density profiles (ADPs) calculated from the centre of mass of micelles containing between 40 and 48 surfactant molecules measured at 25C (lighter lines) and 50C (darker lines). The green lines correspond to the carbon atoms in the surfactant molecules' hydrophobic tail, and the blue lines correspond to the nitrogen atoms in the surfactants' headgroups. While the magenta/purple lines show the location of the bromide counterions and the red lines are the water molecule locations (NB the water ADPs have been scaled up by a factor of 10 for clarity).....36

Figure 32: (a) Colour plots of $f(x,y)$ (b) Transverse line-out of the function under (a) at $x_1=5500$38

Figure 33: Effect of absolute plasma density and density gradient on laser beam propagation. (a) Propagation in the standard channel given by $f(x,y)$. (b) Propagation in the modified channel $2f(x/2,y)$, so the amplitude of the density perturbation is doubled while the density gradients are preserved. (c) Propagation in the modified channel $f(2x,y)$, so the density gradients are doubled while the amplitude of the density perturbation is preserved.40

Figure 34: SCARF Queue Usage47

Figure 35: SCARF-Lexicon Usage48

Figure 36: SCARF Lexicon-2 Usage48

Figure 37: SCARF-IBIS Usage49

Figure 38: SCARF Power Usage49

Figure 39: GFlops/W for SCARF generations of equipment50

Figure 40: Filespace usage on the Panasas Storage50

Figure 41: SCARF Network Topology51

Figure 42: SCARF06, SCARF-Lexicon[1-2], SCARF08, SCARF09 Network Usage.....51

Figure 43: SCARF10 Network Usage52

Figure 44: SCARF11 and SCARF1252

Figure 45: SCARF Application Stack.....53

3. APPENDIX: PUBLICATIONS AND PRESENTATIONS

#	Reference	Department
1.	Pub: "Assignment of metal-ligand modes in Pt(II) diimine complexes relevant to solar energy conversion", S.F. Parker, K. Refson, R.D. Bennett, J. Best, M.Ya. Mel'nikov and J.A. Weinstein, <i>Inorg. Chem.</i> , accepted for publication. [doi: 10.1021/ic3011184]	Stewart Parker (ISIS)
2.	Pub: "Characterisation of C5 hydrocarbons relevant to catalysis", S.F. Parker, D. Siegel, N.G. Hamilton, J. Kapitán, L. Hecht and D. Lennon, <i>J. Phys. Chem. A</i> 116 (2012) 333–346. [doi: 10.1021/jp209417d]	Stewart Parker (ISIS)
3.	Pub: Bell AR, Schure KM, Reville B Cosmic ray acceleration at oblique shocks <i>Monthly Notices of the Royal Astronomical Society</i> 418, 1208 (2011)	AR Bell (Oxford, STFC-CLF)
4.	Pub: Thomas AGR, Tzoufras M, Robinson APL, Kingham RJ, Ridgers CP, Sherlock M, Bell AR A review of Vlasov-Fokker-Planck numerical modeling of inertial confinement fusion plasma <i>Journal of Computational Physics</i> 231, 1051 (2012)	AR Bell (Oxford, STFC- CLF)
5.	Pub: Tzoufras M, Bell AR, Norreys PA, Tsung FS A Vlasov-Fokker-Planck code for high energy density physics <i>Journal of Computational Physics</i> 230, 6475 (2011)	AR Bell (Oxford, STFC- CLF)
6.	Pub: G. Graziano, J. Klimeš, F. Fernandez-Alonso, and A. Michaelides, <i>J. Phys. Condens. Matter</i> , Accepted.	Gabriella Graziano (University College of London), Jiří Klimeš (University College of London), Felix Fernandez-Alonso (ISIS), Angelos Michaelides (University College of London)
7.	Pub: R.E. Williamson et al., "Longitudinal dynamics studies for ISIS upgrades", <i>Proc. PAC09</i> , http://epubs.stfc.ac.uk/work-details?w=50342	Rob Williamson (ISIS)
8.	Pub: R.E. Williamson et al., "High intensity longitudinal dynamics studies for higher energy injection into the ISIS synchrotron", <i>Proc. IPAC11</i> , http://epubs.stfc.ac.uk/work-details?w=60831	Rob Williamson (ISIS)
9.	Pub: R.E. Williamson et al., "High Intensity Longitudinal Dynamics Studies for an ISIS Injection Upgrade", <i>Proc. HB2012</i> , http://epubs.stfc.ac.uk/work-details?w=63542	Rob Williamson (ISIS)
10.	Pub: S. Mukhopadhyay and N. M. Harrison, "Influence of background carriers on magnetic properties of Mn-doped dilute magnetic Si", <i>J. Mag. Mat.</i> 324, 3748 (2012).	Sanghamitra. Mukhopadhyay (ISIS)
11.	Pub: S. Mukhopadhyay, M. W. Finnis and N. M. Harrison, "Electronic Structures and Phonon Free Energies of LaCoO3 using Hybrid Exchange Density Functional Theory", to be published in <i>Phys. Rev. B</i> (2012).	Sanghamitra. Mukhopadhyay (ISIS)
12.	Pub: S. Mukhopadhyay, M. Gutmann, D. Jochym, K. Refson and F. Fernandez-Alonso, "Crystalline Structure and Vibrational Properties of Organic Ferroelectric Croconic Acid : an Investigation using Density Functional Theory", presented in the Joint CMD-24, ECOS-29, ECSCD-11 and CMMP-12 Conference held at Edinburgh, 3-7 September (2012).	Sanghamitra. Mukhopadhyay (ISIS)
13.	Pub: Yang S., Sun J., Ramirez-Cuesta A.J., Calleja S.K., David W.I.F, Anderson D., Newby A., Blake A.J., Parker J.E., Tang C.E. and Schröder M. "Direct Visualisation of Carbon Dioxide and Sulphur Dioxide in a Decorated Porous Host" <i>Nature Chemistry</i> , DOI: 10.1038/NCHEM.1457	AJ Ramirez-Cuesta (ISIS)
14.	Pub: Albinati, A., Colognesi, D., Georgiev, P. A., Jensen, C. M. and Ramirez-Cuesta, A. J. On the effect of thermal treatment and hydrogen vibrational dynamics in sodium alanates: An inelastic neutron scattering study. <i>Journal of Alloys and Compounds</i> 523, 108–113 (2012).	AJ Ramirez-Cuesta (ISIS)
15.	Pub: Queen, WL, Bloch ED, Brown CM, Hudson MR, Mason JA, Murray LJ, Ramirez-Cuesta AJ, Peterson VK, and Long JR. Hydrogen adsorption in the metal-organic frameworks Fe-2(dobdc) and Fe-2(O-2)(dobdc). <i>Dalton Transactions</i> 41, 4180–4187 (2012).	AJ Ramirez-Cuesta (ISIS)
16.	Pub: Celli, M., Colognesi, D., Ulivi, L., Zoppi, M. and Ramirez-Cuesta, A. J. Phonon density of states in different clathrate hydrates measured by inelastic neutron scattering. <i>5th European Conference On Neutron Scattering</i> 340, (2012).	AJ Ramirez-Cuesta (ISIS)
17.	Pub: Borgschulte, A.; Callini, E.; Probst, B.; Jain, A.; Kato, S.; Friedrichs, O.; Remhof, A.; Biemann, M.; Ramirez-Cuesta, A. J.; Zuttel, A., Impurity Gas Analysis of the Decomposition of Complex Hydrides. <i>Journal of Physical Chemistry C</i> 2011, 115 (34), 17220-17226.	AJ Ramirez-Cuesta (ISIS)

18.	Pub: Borgschulte, A.; Jain, A.; Ramirez-Cuesta, A. J.; Martelli, P.; Remhof, A.; Friedrichs, O.; Gremaud, R.; Zuttel, A., Mobility and dynamics in the complex hydrides LiAlH ₄ and LiBH ₄ . Faraday Discussions 2011, 151, 213-230.	AJ Ramirez-Cuesta (ISIS)
19.	Pub: Colognesi, D.; Giannasi, A.; Ulivi, L.; Zoppi, M.; Ramirez-Cuesta, A. J.; Roth, A.; Fichtner, M., Raman and Inelastic Neutron Scattering Study on a Melt-Infiltrated Composite of NaAlH ₄ and Nanoporous Carbon. Journal of Physical Chemistry A 2011, 115 (26), 7503-7510.	AJ Ramirez-Cuesta (ISIS)
20.	Pub: Sato, T.; Ramirez-Cuesta, A. J.; Ikeda, K.; Orimo, S.; Yamada, K., Vibrational Properties of CaAlH ₅ and alpha-AlH ₃ with Different AlH ₆ Networks Studied by Inelastic Neutron Scattering. Inorganic Chemistry 2011, 50 (17), 8007-8011.	AJ Ramirez-Cuesta (ISIS)
21.	Pub: Beam Loss Studies of the ISIS Synchrotron using ORBIT. D.J. Adams. IPAC12	Dean Adams (ISIS)
22.	Pub: Beam Loss Control in the ISIS Accelerator Facility. D.J. Adams HB2012	Dean Adams (ISIS)
23.	Pub: Simulation and Measurement of Half Integer Resonance in Coasting Beams in the ISIS Ring. C.M.Warsop. HB2012	Dean Adams (ISIS)
24.	Pub: Injection and Stripping Foil Studies for a 180 MeV Injection upgrade at ISIS. B. Jones, HB2012	Dean Adams (ISIS)
25.	Pub: A.P.L.Robinson, M.H.Key and M.Tabak, Phys.Rev.Lett, 108, 125004 (2012)	A.P.L.Robinson (CLF)
26.	Pub: A.P.L.Robinson, R.Trines, Z.Najmudin, and N.Dover, Plasma Phys.Control. Fusion, 54, 115001 (2012)	A.P.L.Robinson (CLF)
27.	Pub: M.Quinn et al., Plasma Phys. Control.Fusion, 53,025007 (2011)	A.P.L.Robinson (CLF)
28.	Pub: X.H.Yang et al., Phys.Plasmas, 18, 093102 (2011)	A.P.L.Robinson (CLF)
29.	Pub: G.Chatterjee et al., Phys.Rev.Lett, 108, 235005 (2012)	A.P.L.Robinson (CLF)
30.	Pub: X.H.Yang, M.Borghesi, and A.P.L.Robinson, Phys.Plasmas, 19, 062702 (2012)	A.P.L.Robinson (CLF)
31.	Pub: B. Qiao et al Phys. Rev. Lett. 108, 115002 (2012).	Bin Qiao (QUB), Macro Borghesi (QUB), Matthew Zepf (QUB), David Neely (RAL)
32.	Pub: S. Kar, K.F. Kakolee, and B. Qiao et al., Phys. Rev. Lett. Accepted (2012)	Bin Qiao (QUB), Macro Borghesi (QUB), Matthew Zepf (QUB), David Neely (RAL)
33.	Pub: The effect of temperature on C10TAB micelles, R Hargreaves, DT Bowron and K Edler, Soft Matter, 2013, (in prep.)	Rowan Hargreaves (ISIS)
34.	Pub: The effect of excess salt on C10TAB micelles in solution, Proceedings of Faraday Discussion 167, 2013 (in prep.).	Rowan Hargreaves (ISIS)
35.	Pub: R. Trines, F. Fiúza, et al., "Production of Picosecond, Kilojoule and Petawatt Laser Pulses via Raman Amplification of Nanosecond pulses", Phys. Rev. Lett. 107, 105002 (2011).	E. Higson ^{1,2} , R. Trines ² , R. Bingham ^{2,3} , and P.A. Norreys ^{1,2,4} [1]University of Oxford [2] Central Laser Facility, [3] University of Strathclyde, [4] Imperial College London.
36.	Pub: A. Robinson, R. Trines, J. Polz and M. Kaluza, "Absorption of circularly polarized laser pulses in near-critical plasmas", Plasma Phys. Contr. Fusion 53, 065019 (2011).	E. Higson ^{1,2} , R. Trines ² , R. Bingham ^{2,3} , and P.A. Norreys ^{1,2,4} [1]University of Oxford [2] Central Laser Facility, [3] University of Strathclyde, [4] Imperial College London.
37.	Pub: A. Robinson, R. Trines, N. Dover and Z. Najmudin, "Hole-boring radiation pressure acceleration as a basis for producing high-energy proton bunches", Plasma Phys. Contr. Fusion 54, 115001 (2012).	E. Higson ^{1,2} , R. Trines ² , R. Bingham ^{2,3} , and P.A. Norreys ^{1,2,4} [1]University of Oxford [2] Central Laser Facility, [3] University of Strathclyde, [4] Imperial College London.
38.	Pub: G. Sarri et al., "Employing laser-accelerated proton beams to diagnose high intensity laser-plasma interactions", AIP Conf. Proc. 1462, 149 (2011).	E. Higson ^{1,2} , R. Trines ² , R. Bingham ^{2,3} , and P.A. Norreys ^{1,2,4} [1]University of Oxford [2] Central Laser Facility, [3] University of Strathclyde, [4] Imperial College London.
39.	Pub: R. Scott et al., "A study of fast electron energy transport in relativistically intense laser-plasma interactions with large density scale lengths", Phys. Plasmas 19, 053104 (2012).	E. Higson ^{1,2} , R. Trines ² , R. Bingham ^{2,3} , and P.A. Norreys ^{1,2,4} [1]University of Oxford [2] Central Laser Facility, [3] University of Strathclyde, [4] Imperial

		College London.
40.	Pub: R. Trines, F. Fiúza et al., "Numerical Simulation of Plasma Based Raman Amplification of Laser Pulses to Petawatt Powers", IEEE Trans. Plasma Sci. 39, 2622 (2011).	E. Higson ^{1,2} , R. Trines ² , R. Bingham ^{2,3} , and P.A. Norreys ^{1,2,4} [1]University of Oxford [2] Central Laser Facility, [3] University of Strathclyde, [4] Imperial College London.
41.		
42.	Presentation: "Computer modelling of molecular adsorption at mineral interfaces." J. C. Crabtree, S. C. Parker, T. V. Shapley, L. N. Woronycz, S. Perera, J. Purton, C. Arrouvel, D. Costa. Poster presented at RSC Solid State Chemistry Group Christmas Meeting, 19 th December 2011, University of Liverpool, UK.	J. C. Crabtree, S. C. Parker (University of Bath), J. A. Purton (STFC, Daresbury)
43.	Presentation: "Molecular Adsorption at Mineral Interfaces." L. N. Woronycz, J. C. Crabtree, T. V. Shapley, S. C. Parker. Poster presented at Materials Chemistry Consortium Conference, 29 th March 2012, UCL, UK.	J. C. Crabtree, S. C. Parker (University of Bath), J. A. Purton (STFC, Daresbury)
44.	Presentation: "Zeolites for CO ₂ sequestration: a computational study." J. C. Crabtree, S. C. Parker, J. A. Purton, S. Perera. Talk presented at British Zeolite Association 2012 Annual Conference, 17 th July 2012, University of Chester, UK.	J. C. Crabtree, S. C. Parker (University of Bath), J. A. Purton (STFC, Daresbury)
45.	Presentation: Particle acceleration by shocks Gamma2012 conference, Heidelberg, Germany, July 2012	
46.	Presentation: Vlasov-Fokker-Planck Simulation IOP Computational Plasma Physics Conference, Brighton, UK, Sept 2012	
47.	Presentation: IOP Conference 2012	James Holloway (UCL, STFC-CLF)
48.	Presentation: HPL Conference 2011	James Holloway (UCL, STFC-CLF)
49.	Presentation: Particle Physics Seminar RAL 2011	James Holloway (UCL, STFC-CLF)
50.	Presentation: APS March meeting 2012 Boston 28 th of February-2 nd of March 2012. (Oral presentation)	Gabriella Graziano (University College of London), Jiří Klimeš (University College of London), Felix Fernandez-Alonso (ISIS), Angelos Michaelides (University College of London)
51.	Presentation: 2nd Thomas Young centre energy materials workshop and tutorial. London 6 th -7 th of June (Poster)	Gabriella Graziano (University College of London), Jiří Klimeš (University College of London), Felix Fernandez-Alonso (ISIS), Angelos Michaelides (University College of London)
52.	Presentation: ICTAC-14 Vlissingen (Netherlands) 26 th -30 th of June 2012 (Poster)	Gabriella Graziano (University College of London), Jiří Klimeš (University College of London), Felix Fernandez-Alonso (ISIS), Angelos Michaelides (University College of London)
53.	Presentation: ECOSS-29 Edinburgh 3 rd -7 th of September 2012 (Oral presentation)	Gabriella Graziano (University College of London), Jiří Klimeš (University College of London), Felix Fernandez-Alonso (ISIS), Angelos Michaelides (University College of London)
54.	Presentation: "Neutrons and Computational Models: Prospect from a Scientist from ISIS: Data reduction, analysis and interpretation in neutron scattering", Building an Advanced Center for Data and Computing for ESS, Niels Bohr Institute, Copenhagen, September 17-18, 2012 (Invited)	AJ Ramirez-Cuesta (ISIS)
55.	Presentation: "Studying Small Molecules Adsorption on MOF" ACNS, American Conference on Neutron Scattering, Georgetown, USA, 25 th June 2012.	AJ Ramirez-Cuesta (ISIS)
56.	Presentation: "The power of inelastic neutron Scattering", Neutron Scattering Seminar at the Niels Bohr Institute, University of Copenhagen, Denmark, 11 th May 2012 (Invited)	AJ Ramirez-Cuesta (ISIS)
57.	Presentation: "Data Reduction, Analysis and Interpretation in Vibrational Neutron Spectroscopy, Why Mantid is such a good idea" ESS Data Management Centre (DMC), Niels Bohr Institute, University of Copenhagen, Denmark, 7 th May 2012 (Invited)	AJ Ramirez-Cuesta (ISIS)
58.	Presentation: "Combined INS and DFT studies of Metal Organics Frameworks,	AJ Ramirez-Cuesta (ISIS)

	Probing the interactions of small molecules with the host material", 6th International Symposium Hydrogen and Energy, Stoos, Switzerland, 22-27 January 2012.	
59.	Presentation: "Espectroscopia de Neutrones, Aplicaciones al estudio de materiales hidrogenados" Research seminar at the University of Malaga, Spain, 26th September 2011, (Invited)	AJ Ramirez-Cuesta (ISIS)
60.	Presentation: "Applications of INS to hydrogen storage materials" UK-SHEC hydrogen and fuel cell Researchers Workshop, Bath University 8th September 2011. (Invited)	AJ Ramirez-Cuesta (ISIS)
61.	Presentation: "Ab-Initio Calculations Of The Dynamics Of Select Hydrogen Containing Materials, Compared To Inelastic Neutron Scattering Spectra", Swedish Neutron Scattering Society 2011 Meeting, Gothenburg, August 2011, (Invited).	AJ Ramirez-Cuesta (ISIS)
62.	Presentation: "Studying hydrogen storage materials using Neutron Scattering" ECNS 2011, Prague, 21st July 2011.	AJ Ramirez-Cuesta (ISIS)
63.	Presentation: EPSR at the extremes, R Hargreaves, EPSR Workshop Nov 2011.	Rowan Hargreaves (ISIS)
64.	Presentation: Invited presentation D T Bowron: e-Infrastructure South Centre for Innovation meeting, June 2012.	Rowan Hargreaves (ISIS)
65.	Presentation: Invited talk K Edler: The effect of excess salt on micelle structure, Mesostructure and Dynamics in Liquids and Solutions: Faraday Discussion 167, Sept 2013	Rowan Hargreaves (ISIS)
66.	Presentation: "Production of Picosecond, Kilojoule and Petawatt Laser Pulses via Raman Amplification of Nanosecond pulses", Inertial Fusion Science and Applications conference, Bordeaux, Sept. 2011.	E. Higson ^{1,2} , R. Trines ² , R. Bingham ^{2,3} , and P.A. Norreys ^{1,2,4} [1]University of Oxford [2] Central Laser Facility, [3] University of Strathclyde, [4] Imperial College London.
67.	Presentation: "Production of Intense EM Pulses for Laser Driven Nuclear Fusion and High Energy Density Physics", ITER-IAEA-ICTP Advanced Workshop on Fusion and Plasma Physics, Trieste, October 2011.	E. Higson ^{1,2} , R. Trines ² , R. Bingham ^{2,3} , and P.A. Norreys ^{1,2,4} [1]University of Oxford [2] Central Laser Facility, [3] University of Strathclyde, [4] Imperial College London.
68.	Presentation: "Channelling, Filamentation and Bubble Formation in Laser-Driven Nuclear Fusion", 30th UK Fusion Theory Meeting, Culham Science Centre, Abingdon, November 2011.	E. Higson ^{1,2} , R. Trines ² , R. Bingham ^{2,3} , and P.A. Norreys ^{1,2,4} [1]University of Oxford [2] Central Laser Facility, [3] University of Strathclyde, [4] Imperial College London.
69.	Presentation: "Production of Picosecond, Kilojoule and Petawatt Laser Pulses via Raman Amplification of Nanosecond pulses", 53rd Annual Meeting of the APS Division of Plasma Physics, Salt Lake City, November 2011.	E. Higson ^{1,2} , R. Trines ² , R. Bingham ^{2,3} , and P.A. Norreys ^{1,2,4} [1]University of Oxford [2] Central Laser Facility, [3] University of Strathclyde, [4] Imperial College London.
70.	Presentation: "Channelling and filamentation in laser-driven nuclear fusion", Christmas High Power Laser Science Community Meeting, Abingdon, December 2011.	E. Higson ^{1,2} , R. Trines ² , R. Bingham ^{2,3} , and P.A. Norreys ^{1,2,4} [1]University of Oxford [2] Central Laser Facility, [3] University of Strathclyde, [4] Imperial College London.
71.	Presentation: E. Higson, "The role of wave front deformation in laser-beam filamentation", Christmas High Power Laser Science Community Meeting, Abingdon, December 2011.	E. Higson ^{1,2} , R. Trines ² , R. Bingham ^{2,3} , and P.A. Norreys ^{1,2,4} [1]University of Oxford [2] Central Laser Facility, [3] University of Strathclyde, [4] Imperial College London.
72.	Presentation: "Raman compression of long laser pulses to picosecond duration for fast-ignition fusion and high energy density physics", Third International Workshop on Laser-Matter Interaction, Porquerolles (France), June 2012.	E. Higson ^{1,2} , R. Trines ² , R. Bingham ^{2,3} , and P.A. Norreys ^{1,2,4} [1]University of Oxford [2] Central Laser Facility, [3] University of Strathclyde, [4] Imperial College London.
73.	Presentation: "Raman amplification of laser pulses to multi-petawatt powers in plasma", 39th EPS Conference on Plasma Physics, Stockholm, July 2012.	E. Higson ^{1,2} , R. Trines ² , R. Bingham ^{2,3} , and P.A. Norreys ^{1,2,4} [1]University of Oxford [2] Central Laser Facility, [3] University of Strathclyde, [4] Imperial College London.

4. APPENDIX: SCARF QUEUE USAGE 2011-12

A new reporting tool was deployed in May 2012 and hence there is no data before that period

Key:

- **Red - number of jobs pending**
- **Green - number of jobs running**
- **yellow - number of jobs gathering CPUs so that they can run (large parallel jobs)**
- **Blue - total number of Jobs (sum of Red, Green, Yellow)**

4.1 General SCARF Queue

Open to all SCARF Users with a capacity of ~1400 CPU cores

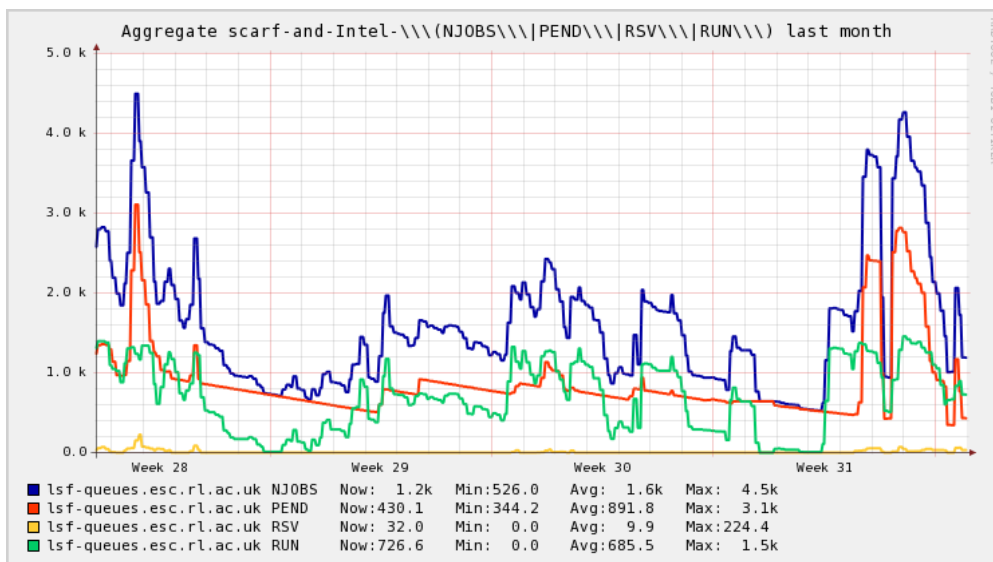
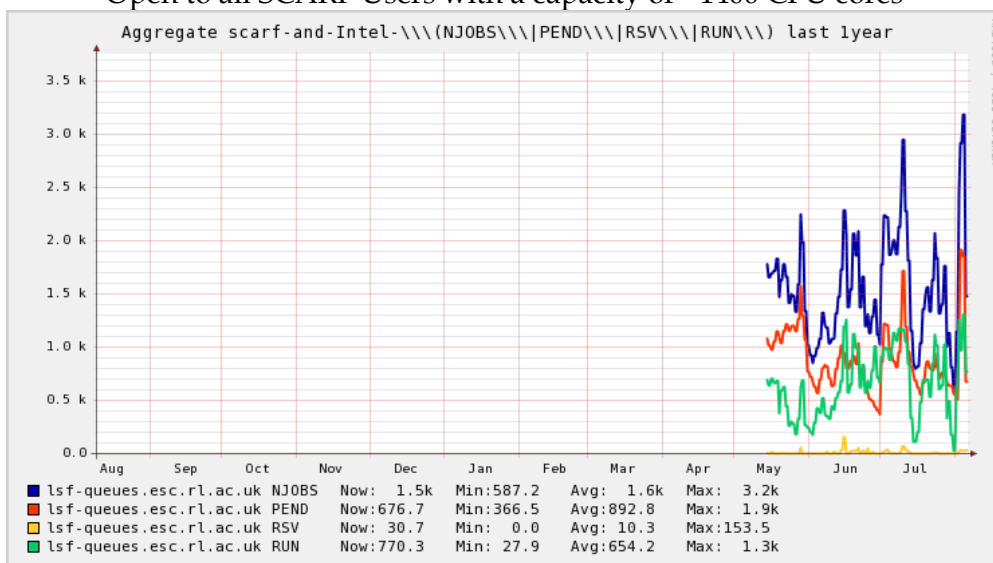


Figure 34: SCARF Queue Usage

The graph for the SCARF queue (and thus the combined SCARF/INTEL graph) shows consistently pending jobs for most of the year, which demonstrates that there is not sufficient capacity. This should be addressed by the next hardware procurement.

4.2 SCARF-Lexicon[1-2] Queues

These queues are primarily for CLF use with a capacity of 292 and 544 CPU cores for SCARF Lexicon 1 & 2 respectively.

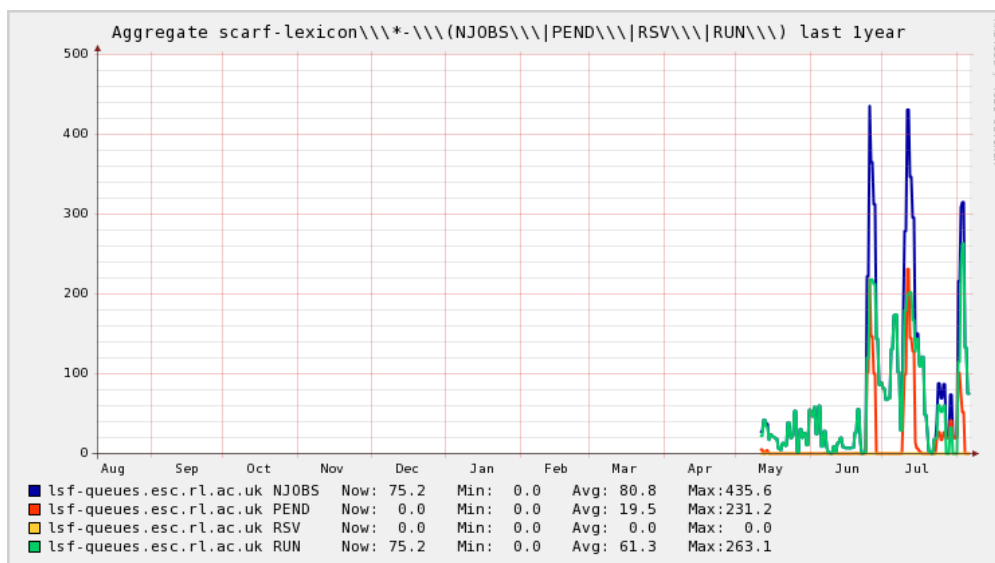


Figure 35: SCARF-Lexicon Usage

The graph for the SCARF-LEXICON queue shows peaky but significant usage, though this has dropped somewhat since the purchase of SCARF-LEXICON-2.

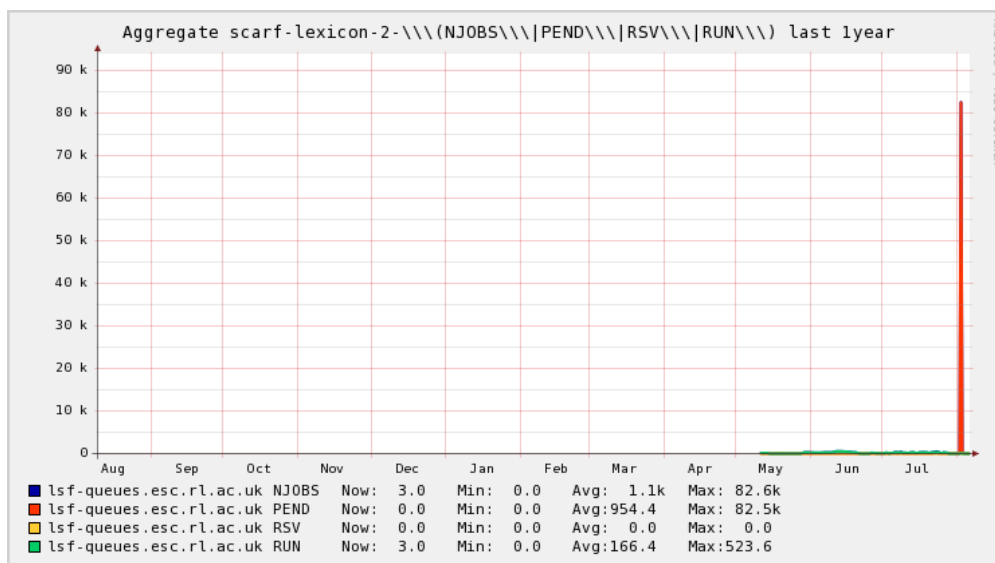


Figure 36: SCARF Lexicon-2 Usage

SCARF-LEXICON-2 is dominated by a large study from a user who submitted several hundred thousand jobs.

4.3 SCARF-IBIS

SCARF-IBIS has a capacity of 144 CPU cores.

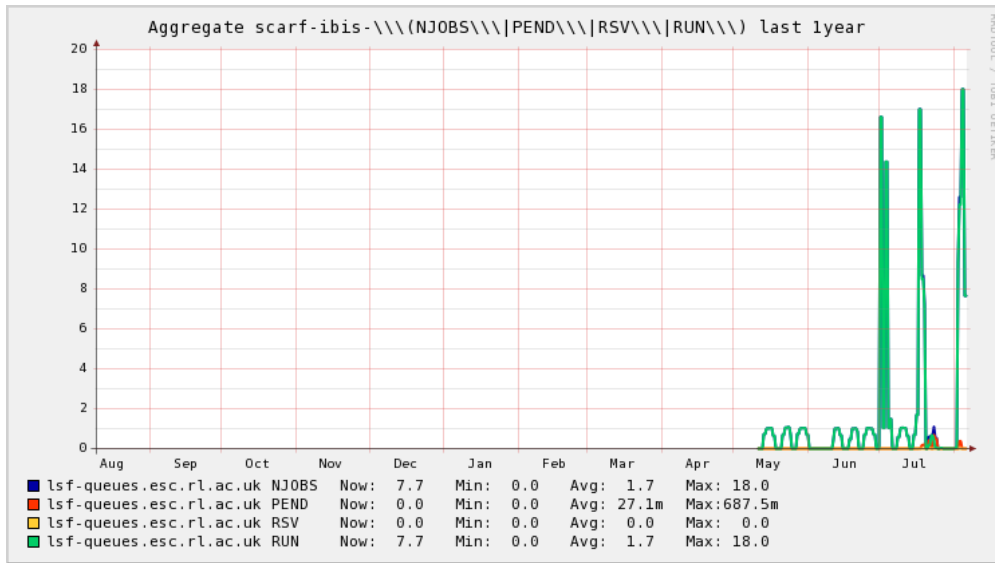


Figure 37: SCARF-IBIS Usage

4.4 SCARF Total Power draw (amps)

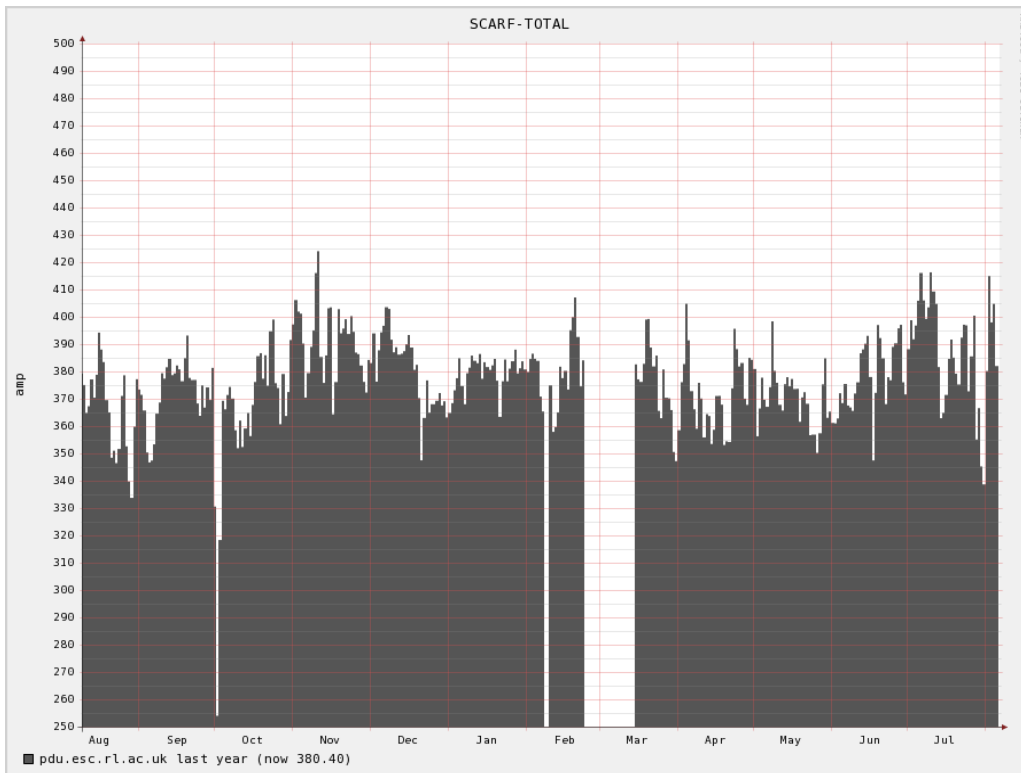


Figure 38: SCARF Power Usage

The approximate average power draw of the SCARF cluster (including Lexicon) is about 380 amp or 91kW/hr. This excludes the power needed to cool, pump and move cold air. The efficiency of SCARF in terms in Gflops/W is giving in the table below.

Year Purchased	Gflops/W
2006	0.07
2007	0.09
2008	0.21
2009	0.29
2010	0.32
2011	0.48
2012	0.50

Figure 39: GFlops/W for SCARF generations of equipment

From the above table it is clear that the Gflops/W achieved increase per generation of the SCARF equipment. This supports the continual refresh rate of SCARF hardware rather than a big bang approach.

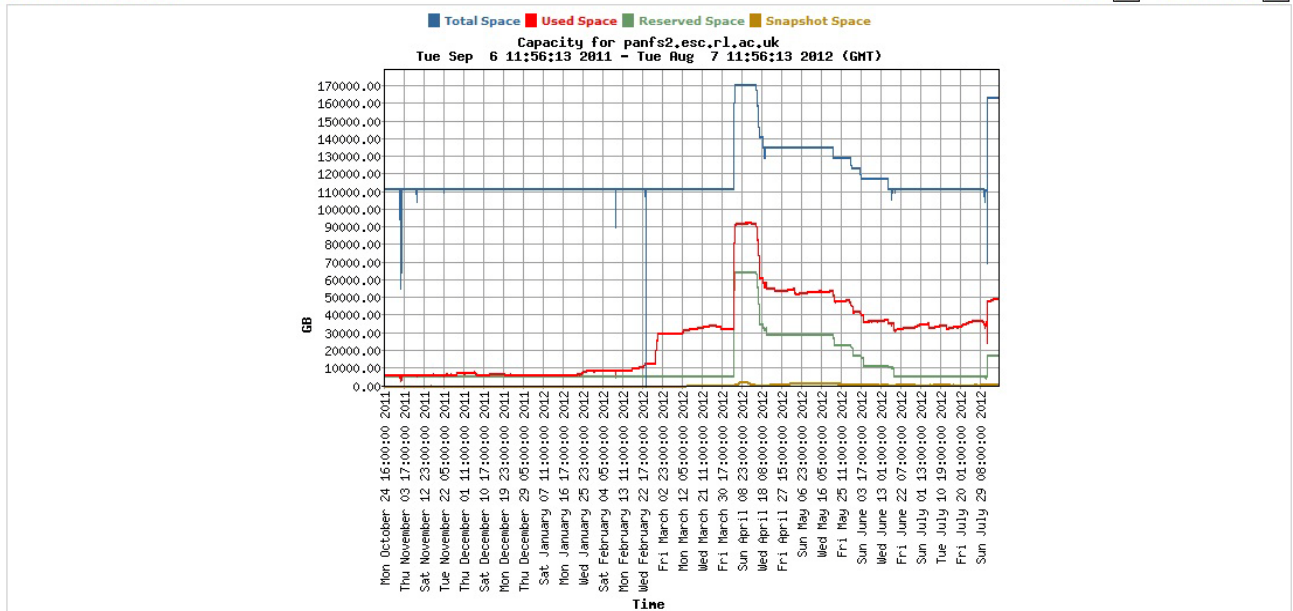
4.5 Filesystem Usage

The plot below outlines the use of the Panasas filesystem on the SCARF service. In Oct 2011 new hardware was procured and the migration of data took place during the Jan - March 2012. The Panasas storage was merged with the storage from the EMERALD GPU resource creating a larger and more performance system for both projects. Initial deployment issues (see section 1.2) have meant that the combined storage of 5 shelves (2 SCARF and 3 EMERALD) is not yet fully available.

panfs2.esc.rl.ac.uk System Capacity Report

Date: From (09/06/2011)

Export Printable View



Page generated: 11:56:13 August 07, 2012

Terms & Conditions : Site Map : Home

Copyright 2012 Panasas Inc. All rights reserved.



Figure 40: Filespace usage on the Panasas Storage

4.6 Networking

The diagram below shows the SCARF compute clusters embedded in the larger Scientific Computing Technology group’s networking infrastructure.

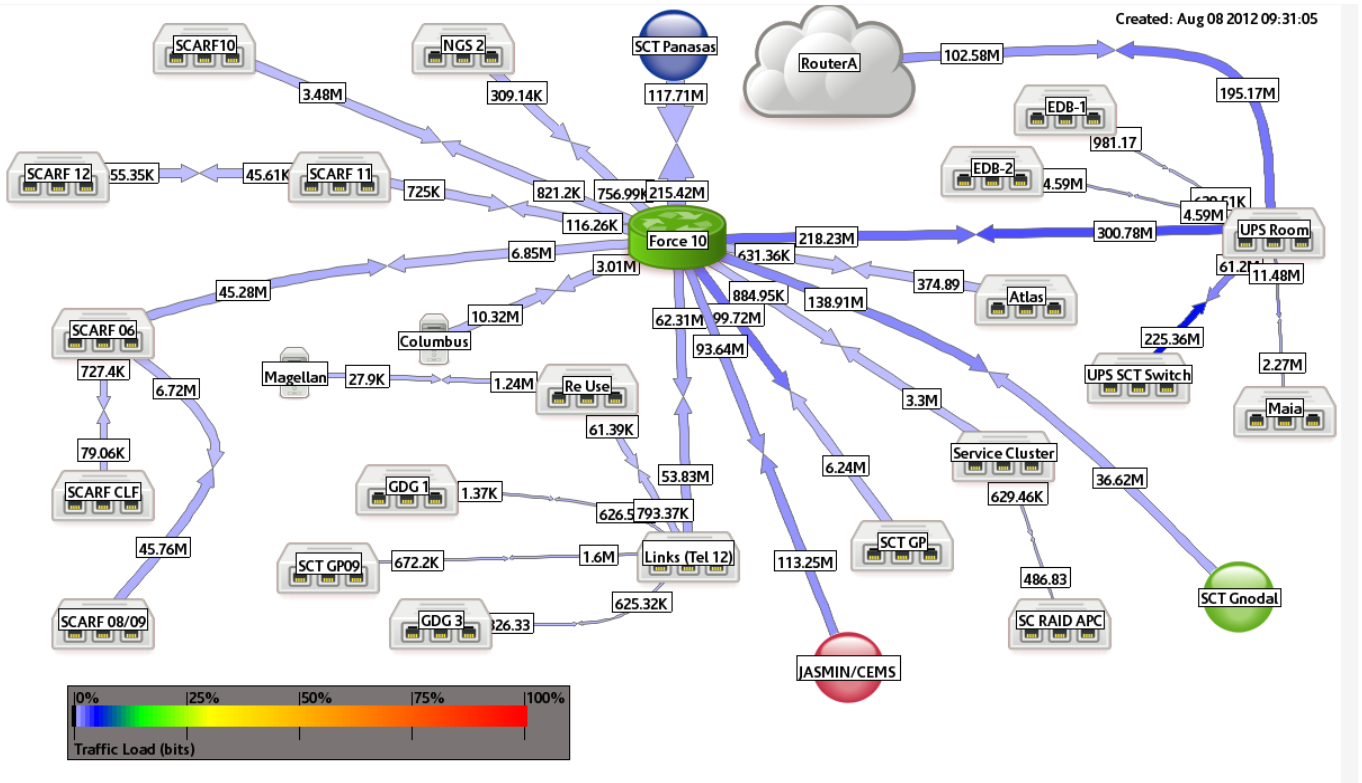


Figure 41: SCARF Network Topology

The following graphs outline the network traffic from the clusters. This captures traffic to the Panasas filesystems, backups external traffic.

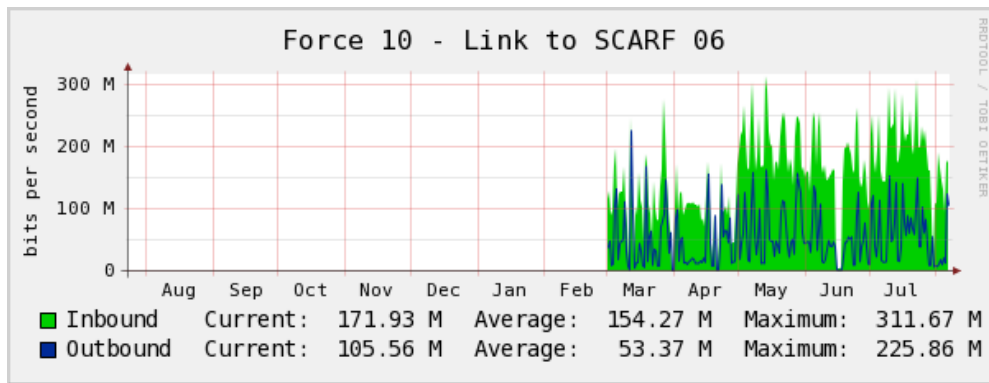


Figure 42: SCARF06, SCARF-Lexicon[1-2], SCARF08, SCARF09 Network Usage

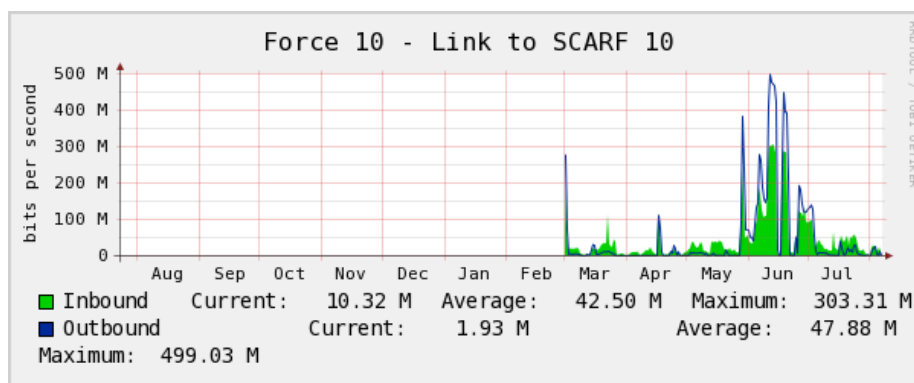


Figure 43: SCARF10 Network Usage

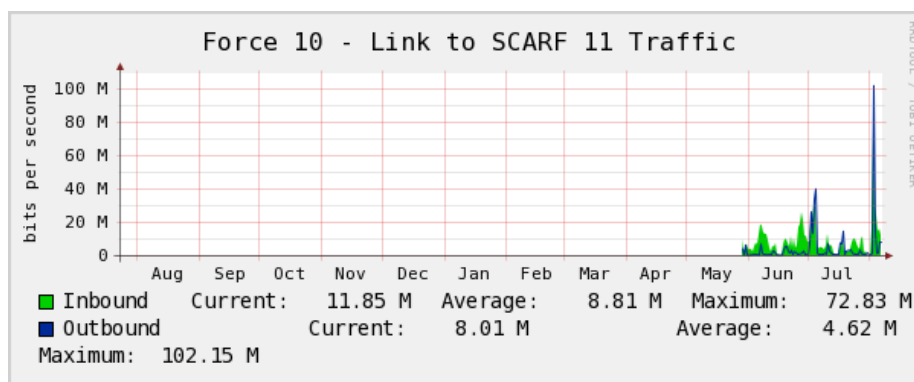


Figure 44: SCARF11 and SCARF12

5. APPENDIX – SCARF DEVELOPMENTS

It has been a busy year for the SCARF service. Users’ will have noticed most impact with the additional of capacity and upgrades to applications. However, a lot of effort goes into improving the management of SCARF. SCARF is also part of NGS which allows users to use grid technology to access a larger pool of resources.

5.1 Technical Developments

- The completion of the migration of the cluster nodes to RedHat 5 and LSF8 was completed in early August 2011,
- In Mid March the 2012 hardware tranche of 20 dual Intel x5675 nodes, providing 240 cores, was made available to users
- Also in mid March, we reorganised the layout of users' home directories moving from storing them in one volume in our Panasas system to a volume per user group. This allowed us to parallelise the backup of home directories reducing the amount of time spent backing them up.
- This migration of user's home directories also included a migration to 2 new Panasas ActiveStore 11 shelves, replacing the existing PAS-8 shelves, allowing us to increase the minimum home directory quota to 100GB per user.

- As part of an separate project, 3 new Panasas shelves were purchased, and are being integrated with the 2 existing shelves, this will increase the bandwidth to storage from 20Gb/s to 50Gb/s, due distribution of data across all 5 shelves
- The rack containing the SCARF11 nodes was moved from its original position in the machine room to next to the SCARF12 rack - this will give us the potential to connect SCARF10,11,12 into the same infiniband network in the future.

5.2 Application Stack

New or updated applications are in the table below:

Application	Area	Version
ABAQUS	Engineering	6.11-1
CASTEP	Computational Chemistry	6.0
DL_POLY	Computational Chemistry	4.03
Visit	Interactive Visualisation	2..5
HDF5 Parallel version	data model, library, and file format for storing and managing data	1.8.8
Emboss	Molecular Biology	6.4.1
Intel compiler	Fortran, C, C++ compilers and Maths libraries	12.1
PGI compilers	Fortran, C, C++ compilers and Maths libraries	11.8

Figure 45: SCARF Application Stack

5.3 Staff Movements

Derek Ross is the Primary SCARF manager and Ahmed Sajid joined in July to be the secondary manager and assist in hardware support.